Universität Bonn

Institut für Angewandte Physik

Controlling atom transport in a two-dimensional state-dependent optical lattice

Max Werninghaus

Dieser Forschungsbericht wurde als Masterarbeit von der
Mathematisch-Naturwissenschaftlichen Fakultät der Universität Bonn angenommen.

Angenommen am:	11.05.2017
1. Gutachter:	Prof. Dieter Meschede
2. Gutachterin:	Prof. Martin Weitz

Contents

Abstract

This thesis describes the development of an optical phase lock loop on a digital platform, in order to realize state-dependent transport on a two-dimensional optical lattice. The digital platform consists of a field programmable gate array in combination of a vector generator module, which is used to steer the amplitude and phase of the optical lattice deterministically. The digital system enables the implementation of a feedforward control scheme based on internal model control, which overcomes the bandwidth limitations of feedback systems. The control bandwidth is shown to be increased by more than an order of magnitude, directly improving the number of coherent operations that can be executed with the atoms in the optical lattice. The system is implemented into the optical setup of the experimental apparatus, and the first signatures of state-dependent transport of atoms in the two-dimensional optical lattice is observed and presented.

Introduction

The concept of quantum mechanics arose in the beginning of the 20^{th} century and has been continuously investigated since then. The continuous effort towards understanding the fundamental laws has lead to theoretical as well as technological revolutions. One of the most significant was certainly the invention of the first laser in the year 1960 [1], following the idea of Charles H. Townes and Arthur L. Shawlow [2]. The laser paved the way for trapping and cooling techniques that allow to reduce the thermal energy to prepare atomic ensembles of the motional ground state [3, 4]. This led, for example, to the first observation of a Bose-Einstein-Condensate in 1995 [5, 6] – a quantum state of matter formed by bosonic particles when approaching a high phase space density – that was predicted by A. Einstein and S. Bose in 1924 [7, 8, 9].

The laser is also an important building block in realizing quantum simulations, a concept proposed in 1985 by Richard P. Feynman [10], who suggested to use tunable quantum systems to mimic the Hamiltonian of a desired system. This way, the dynamics of the system can be simulated efficiently, since the quantum mechanical interactions are intrinsically provided by the quantum nature of the simulator. Besides simulating known matter – such as electrons in solid state materials [11] – tunable quantum systems further allow to explore artificial quantum matter, e.g. topological insulators [12].

The quantum system which is in the focus of this thesis consists of cold atoms trapped in a state-dependent optical lattice potential. Optical lattices offer a quantum mechanical system which is remarkably tunable, while also allowing to access the quantum state of each individual particle, by e.g. fluorescence imaging [13, 14]. They can thereby serve as a model system for investigating fundamental theoretical concepts and quantum many-body effects [15]. Besides the tunability and the accessibility, cold atoms in optical lattices have the advantage of scalability. Interfering laser beams create lattices with more than a thousand lattice sites, while being able to control depth and dynamics to a great amount. In our experiment in Bonn we follow the bottom-up approach, where we steer the quantum mechanical behavior of single atoms directly. State-of-the-art techniques are employed to manipulate the position of neutral Cesium atoms depending on their internal state, in order to study few atom physics [16]. The building block of our research is the quantum walk, i.e. the quantum mechanical equivalent of the classical random walk. Quantum walks find large number of applications for quantum simulation of different gauge fields, spontaneous equlilibration, and thermalization [17]. In previous work, our group used quantum walks in one dimension to e.g. simulate the effect of electric fields on charged paricles in lattice potentials [15], and observed a violation of the Leggett-Garg-Inequality using ideal negative measurements [18]. For detailed information on the one dimensional experimental setup see Robens [14]. A promising application of two-dimensional quantum walks is the investigation of topological phenomena like artificial magnetic fields and topologically protected edge states [19]. Just recently, the Nobel prize was partially awarded to David J. Thouless for his work on-* combining quantum mechanics with topological concepts to explain the quantum Hall effect [20]. However, experimental realizations of quantum walks have

so far been limited to only one spatial dimension [21, 22, 23]. In our group the construction of a new experimental apparatus using neutral atoms in a state dependent optical lattice is currently under way, which allows the realization of quantum walks in two spatial dimensions.

In general quantum walks require two operations, the so-called *coin*- and the *shift*-operator. The coin operator generates an arbitrary superposition of the internal states, whereas the shift operator is given by a state dependent translation of the two internal states in opposite direction. For ultracold atoms in optical lattices we can realize the former using microwave radiation to couple the two pseudo spin states. However, the shift-operator requires more experimental effort. By utilizing a specifically chosen wavelength, each of the spin states are confined by only one of two perpendicular polarization-components of the light field. Therefore, they can be transported independently from each other by introducing spatial shifts between the sublattices of different polarization [13]. Since a quantum walk requires the coherent interference of all trajectories it is important to transport the atoms as fast as possible without creating excitations, to avoid decoherence of the quantum superposition. In previous work by our group this has been achieved with the so-called *bang-bang* method, where atoms are accelerated and decelerated instantly by changing the phase of the standing wave pattern. Recent theoretical investigations suggest that we can decrease the transport time further using optial control theory [24, 25]. In the scope of this thesis I will implement and characterize a digital stabilization and control unit for phase and amplitude of two optical lattice beams, with the goal to realize state dependent transport in two dimensions. The ability of a purely digital system to further implement an internal-model based feedforward algorithm – which results in a drastic increase of control speed – is an advantage compared to the analog system, and will be the second goal of this thesis.

Outline

The content of this thesis is divided into four parts: In chapter one I will describe the experimental techniques and scientific principles used to realize transport in state-dependent optical lattices in two dimensions.

The second chapter is dedicated to introducing the digital device platform and a characterization of its basic properties.

In the third chapter I will give an overview of control theory with a focus on the fundamentals of feedback control. In addition, I will explain the implementation of the control loops on the digital system in the second part of the chapter. At the end of this chapter, I will present how an internal model control of the lattice can be implemented on the digital platform.

The experimental results onm, state-dependent transport are presented in the last chapter. Furthermore, I will give an outlook of future milestones of the two-dimensional quantum walk experiment.

CHAPTER 1

A two-dimensional optical lattice and state-dependent transport

In this chapter I will briefly introduce the techniques used in the experimental apparatus to realize an optical lattice potential in combination with the ability of state-dependent transport. Detailed information on the experimental setup and the theoretical background can be found in references [13, 14, 26, 27].

1.1 Optical lattice potentials in two dimensions

The trapping force we use to confine our atoms in space is caused by AC-starks shift of the atomic transitions that occurs during the interaction of an atom with a non-resonant light field. The induced dipole moment in the atom results in an attractive force to regions with high light intensity in the case of red detuned light. If the atom transition frequency is larger than the one of the light field (blue detuned), the atom will be repelled from regions of high intensity. Typically, trapping potentials are created by a static intensity pattern created by the interference two counter propagating laser beams. This intensity pattern can be directly calculated by describing the electrical field $\vec{E}$ of each laser beam as

$$\vec{E}_{1,2}(\vec{x},t) = \hat{e}E_0 \exp(\pm\vec{k}\vec{x} - i\omega t), \tag{1.1}$$

where E_0 is the amplitude, $\hat{e}$ is the normalized polarization vector of the electric field, and ω is the light field angular frequency. Here we have neglected the Gaussian beam profile for simplicity by using the plane wave approximation. Choosing the ideal one-dimensional case along the x_1-direction with wave vector $\vec{k}_1 = \hat{x}_1 \frac{2\pi}{\lambda}$, where λ is the wavelength of the light; the static intensity pattern amounts to

$$I_1(x_1) = c_0\epsilon_0 \left| \sum_{i=1,2} \vec{E}_{\mathrm{i}}(\vec{x},t) \right|^2 = I_0 \cos^2(kx_1), \tag{1.2}$$

with $I_0 = 4c_0\epsilon_0 E_0^2$ and $k = 2\pi/\lambda$. The intensity pattern is illustrated in figure 1.1 a. Due to the dipole force this results in a periodic potential for the atoms along the beam propagation axis x_1, with a periodicity of $\lambda/2$.

Introducing a constant phase offset $\exp(i\phi)$ to the field of one of the beams causes a phase-shift

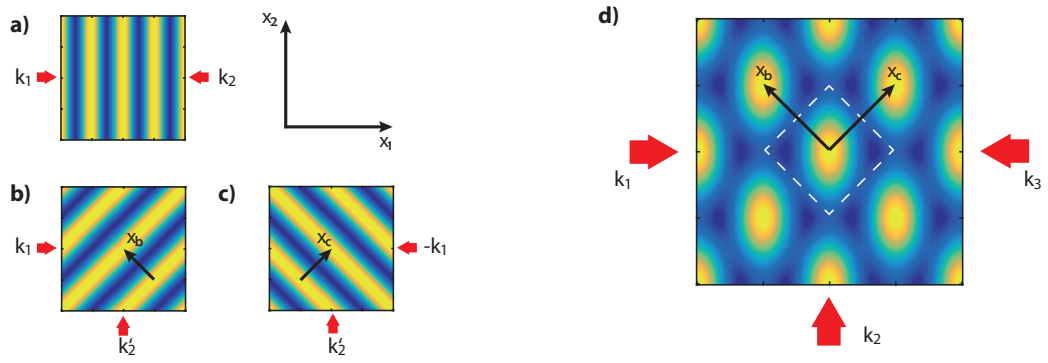

Figure 1.1: Illustration of the one-dimensional lattices caused by the two beam interference. Areas of high intensity are displayed in yellow, while those with low intensity are plotted in blue. a) shows the standard standing wave potential in one dimension and b) shows the interference pattern for a 90° angle between the two interfering beams. c) shows the mirrored situation to b), where one of the beam paths in x_1-direction is inverted. d) Intensity pattern of the full three beam interference. the white dashed square marks the edges of the unit cell. The translation directions $x_{\mathrm{b,c}}$ are indicated by black arrows.

and therefore a translation of the standing wave potential. Changing the phase over a range of 2π corresponds to a translation of one lattice site by

$$\Delta x_1 = \frac{\lambda}{2}\frac{\Delta\phi}{2\pi}. \tag{1.3}$$

A similar interference effect occurs when we choose the two beams to be perpendicular to one another. Figure 1.1 b shows the interference of two beams where $\vec{k}_2 = \hat{x}_2\frac{2\pi}{\lambda}$ is oriented along the x_2 direction, resulting in a one-dimensional potential rotated by 45°. The orientation of the lattice depends on the relative orientation of the interfering beams. Reverting the direction of one of the beams, such that $\vec{k}_1 \to -\vec{k}_1$, and calculating the resulting intensity pattern when interfering with $\vec{k}_2$ yields the orthogonal potentials

$$I_{\mathrm{b,c}}(x_1, x_2) = I_0 \cos^2\left(\frac{k}{2}(x_2 \mp x_1)\right), \tag{1.4}$$

shown in figure 1.1 b and c. The result are periodic intensity patterns along the directions

$$\hat{x}_{\mathrm{b,c}} = \frac{1}{\sqrt{2}}(\mp 1, 1, 0), \tag{1.5}$$

with a rescaled lattice constant of $\lambda/\sqrt{2}$. To extend this concept to a two-dimensional lattice, a combination of three beams with $\vec{k}_1, \vec{k}_2'$ and $\vec{k}_3 = -\vec{k}_1$ is chosen as shown in figure 1.1 d [13]. The resulting intensity pattern can be understood as the sum of the three two-beam potentials. The two-dimensional lattice vectors are defined by the orthogonal intensity patterns defined by equation 1.4. The three beam interference causes a slight elliptical distortion of the intensity maxima, however, the orthogonality of the lattice vectors is preserved.

Performing spatial translations along the vectors $\hat{x}_{\mathrm{b,c}}$ can be achieved by introducing phase

differences between the $\vec{k}_{1,3}$ beams with respect to $\vec{k}_2$

$$\begin{aligned} x_{\mathrm{b}}(t) &= \frac{\lambda}{\sqrt{2}}\frac{\phi(t)}{2\pi}, \\ x_{\mathrm{c}}(t) &= \frac{\lambda}{\sqrt{2}}\frac{\Theta(t)}{2\pi}, \end{aligned} \tag{1.6}$$

where $\phi(t)$ is the phase modulation of $\vec{k}_1$ and Θ is the phase modulation of $\vec{k}_3$. This way, the lattice can be positioned in any arbitrary location in the two-dimensional plane [13]. The confinement and transport of the atoms can be understood as a combination of one-dimensional potentials

$$\begin{aligned} U_1(t) &= U_0 \cos^2\left(k\left[x_{\mathrm{b}} + x_{\mathrm{b}}(t)\right]\right) \\ U_2(t) &= U_0 \cos^2\left(k\left[x_{\mathrm{c}} + x_{\mathrm{c}}(t)\right]\right). \end{aligned} \tag{1.7}$$

Atoms trapped in the potential minima have – due to molasses cooling – typically a temperature of a few tens of microkelvins [14, 28]. For potential depths of in the order of a hundred microkelvin the trapped atom can be well approximated by a harmonic oscillator model [29], for which it is convenient to define the atomic oscillation frequency and an energy scale of vibrational quanta. The trap frequencies in the two-dimensional lattice along the directions x_2 are expected to be equal to a the ones of the one-dimensional lattice setup

$$\omega_1 = \omega_{1\mathrm{D}} = \sqrt{\frac{4\pi U_0}{\lambda\, m_{\mathrm{Cs}}}} = 110\,\mathrm{kHz}. \tag{1.8}$$

The trap frequencies in the x_1 dimension are, due to the elliptical distortion caused by the three beam setup, decreased to be $\omega_2 = \omega_1/\sqrt{3}$ [13]. The trap frequency ω_{tr} in the directions $x_{\mathrm{b,c}}$ are somewhere in between these values, due to the elliptical trap shape. The energy quantization of the atoms, which is a representation of the temperature, is then given in vibrational states $(n+1)/2 \times \hbar\omega_{\mathrm{tr}}$. Even though there is no ground state cooling up to this point of the development of the experimental setup, this description is helpful to describe the heating effects caused by noise and transport operations in section 1.3.

1.2 State dependent trapping potentials for cesium atoms

The most important feature of the two-dimensional discrete quantum walk experiment is to address atoms depending on their internal spin state. This technique is by now well known in our group and has been used to realize a single atom interferometer [30], as well as a low entropy ensemble of atoms [31].

The simple picture of light-matter interactions for dipole forces (red, blue detuning) needs to be modified needs to be modified for real world atoms where fine and hyperfine structure as well as multiple transitions play a crucial role. To understand the spin dependent trapping force, we can refer to the energetic structure of the cesium spin states of the fine-structure depicted in figure 1.2 a. The focus lays on the $^2\mathrm{S}_{1/2}$ ground state of cesium and the first excited states $^2\mathrm{P}_{1/2}$ and $^2\mathrm{P}_{3/2}$. The corresponding cesium D_1 and D_2 transitions are of the wavelengths 894.6 and 852.3 nm [32]. By choosing the lattice wavelength to lay between these transitions, the dipole force of the $^2\mathrm{P}_{3/2}$ excited states with $m_J = \pm 1/2$ is canceled out by the corresponding $^2\mathrm{P}_{1/2}$ states. If the lattice beams are circularly polarized, the light interactions are further limited to

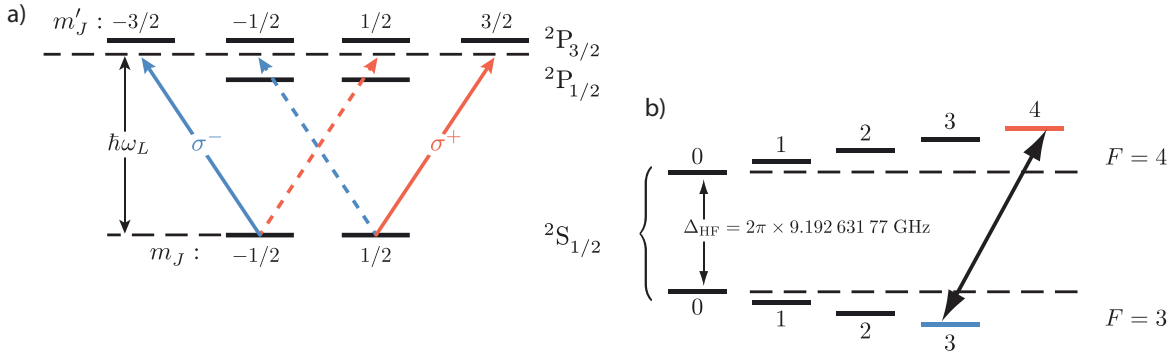

Figure 1.2: a) Fine structure representation of the cesium ground state. The angular light frequency ω_L denotes the frequency for which the potential contributions of the $m_J = \pm 1/2$ magnetic sub levels of the two excited states cancel out. b) Hyperfine structure of the $^2S_{1/2}$ cesium ground state including the two outermost Zeeman sates (red, blue) which define our pseudo-spin 1/2 system.

σ^+ and σ^- transitions. This restricts the two ground states

$$|-\rangle = |J = 1/2, m_J = -1/2\rangle \qquad \text{and} \qquad |+\rangle = |J = 1/2, m_J = +1/2\rangle,$$

to interact almost exclusively with σ^- and σ^+ polarized light, respectively.

The quantization axis is in this case defined by the magnetic field vector, which is aligned with one of the lattice beams. In the experiment presented in this thesis we encode our qubit in the outermost hyperfine states split by the interaction with the magnetic field. Due to the nuclear spin of $I = 7/2$, the $^2S_{1/2}$ ground state is split into spin states with $F = 4$ and $F = 3$, of which we choose the qubit states

$$|\downarrow\rangle = |F = 3, m_F = 3\rangle \qquad \text{and} \qquad |\uparrow\rangle = |F = 4, m_F = 4\rangle. \tag{1.9}$$

It is noteworthy, that in this case the $|\downarrow\rangle$ state is not purely a product of the $m_J = +1/2$ ground state, but instead a superposition with contributions from both ground states:

$$|\downarrow\rangle = \sqrt{\frac{7}{8}}|I = 7/2, m_I = 7/2\rangle \otimes |-\rangle \quad - \quad \sqrt{\frac{1}{8}}|I = 7/2, m_I = 5/2\rangle \otimes |+\rangle \tag{1.10}$$

Thus, our choice of qubits do not allow for a true separation of the two states, as one experiences also a small contribution from the other respective sub-lattice. However, the resulting modulation modulation of the σ^- potentials during transport operations can safely be neglected for the rest of this thesis [13].

State transitions in the two level system can be driven by resonant microwave pulses at the splitting frequency of $\nu_{HF} = 9.192\,\text{GHz}$ [26], but has not yet been implemented in the experimental apparatus. The state dependent lattices can be achieved by synthesizing the counter-propagating lattice beams from σ^+ and σ^- polarized light, a technique that will be introduced in more detail in the next section. The orthogonal reference beam is of static linear polarization, which can be decomposed into equal parts of $\sigma^\pm$ polarized light for our choice of quantization axis as well, which leads to two independent sub-lattices of orthogonally circular polarized light; each of which serves as confinement for one of the qubit states.

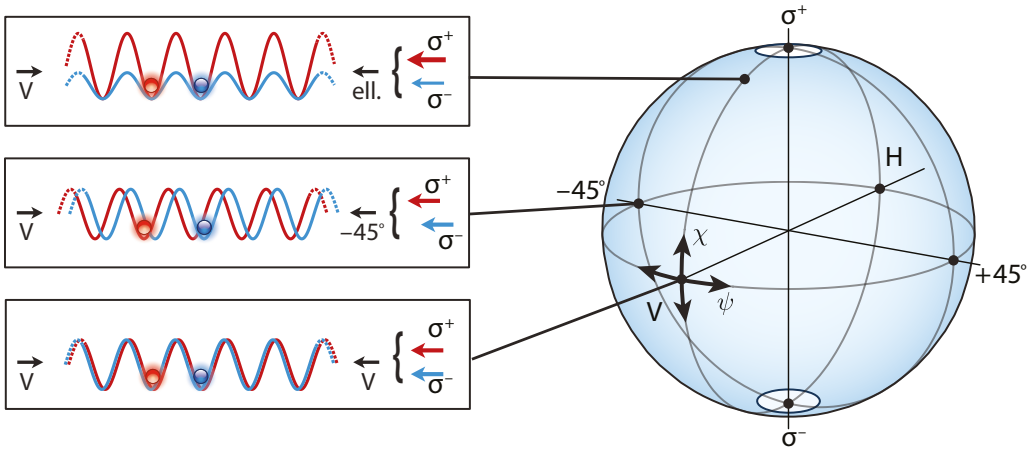

Figure 1.3: Poincaré representation of the polarizations that can be achieved by varying the amplitudes and phases of the orthogonal polarized light fields σ_+ and σ_-. The resulting relative position and depth of the state dependent optical lattices in one dimension is schematically drawn for three distinct points on the Poincaré sphere. This figure has been adapted from [31].

1.3 Two-dimensional state dependent transport through polarization synthesis

In the previous section we established that, in order to store atoms of differing spin states in independent optical lattices, the polarizations of the light fields need to be orthogonally circular. Translations of the respective lattices along the two directions $\hat{x}_{\mathrm{b,c}}$ are achieved by introducing a phase difference between the lattice beams $\vec{k}_1$ and $\vec{k}_3$ with respect to the reference beam $\vec{k}_2$.

To achieve state dependent transport in two dimensions, the two counter propagating beams are synthesized such that

$$\begin{aligned}\vec{E}_1(\vec{x},t) &= \frac{1}{\sqrt{2}}\left[E_\uparrow e^{i\phi_\uparrow}\mathbf{e}_{\sigma^+} + E_\downarrow e^{i\phi_\downarrow}\mathbf{e}_{\sigma^-}\right] e^{i(kx_1-\omega t)},\\ \vec{E}_3(\vec{x},t) &= \frac{1}{\sqrt{2}}\left[E_\uparrow e^{i\Theta_\uparrow}\mathbf{e}_{\sigma^+} + E_\downarrow e^{i\Theta_\downarrow}\mathbf{e}_{\sigma^-}\right] e^{i(kx_1-\omega t)}, \text{ with } \mathbf{e}_{\sigma^\pm} = \frac{1}{\sqrt{2}}\begin{pmatrix}1\\ \pm i\end{pmatrix};\end{aligned} \tag{1.11}$$

consisting of two light fields of circular polarization $\mathbf{e}_{\sigma^\pm}$ with well defined amplitude $E_{\uparrow,\downarrow}$ and phases $\phi_{\uparrow,\downarrow}, \Theta_{\uparrow,\downarrow}$. This enables spatial translations of the two sub lattices as described by equation 1.6. The experimental setup to realize such a synthesized polarization is presented in detail in a recent publication by our group [27].

Applying a phase ramp, e.g. $\phi_\uparrow(t) \propto t$ changes the relative phase $\Delta\phi = \phi_\uparrow - \phi_\downarrow$ between the two polarization components, and results for equal amplitudes $E_\uparrow = E_\downarrow$ in a rotating linear polarized light field, represented by the polar angle $\psi = 2\Delta\phi$ on the Poincaré sphere (see fig. 1.3). If the phase difference for the perpendicular reference beam is kept constant $\Delta\phi = 0$, the lattice confining the $|\uparrow\rangle$ states is translated in the respective direction. The first implementation of such a state dependent lattice was, because of this analogy, utilizing an electro-optic modulator to achieve state dependent transport [26, chapter 4.3]. In the latest approach the setup was revisited and replaced by a synthesis of the light from two independently controlled light beams by acousto-optic modulators [14, 27]. This allows for additional control over the amplitudes of

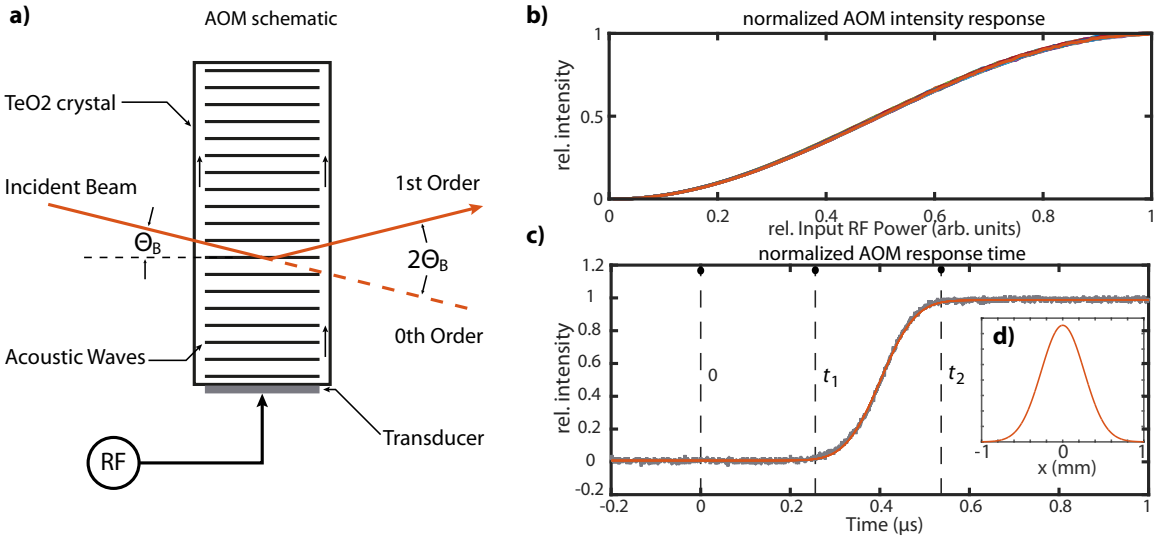

Figure 1.4: a) Schematic drawing of the AOM and the beam path propagation. The Bragg-angle between the incident beam and the moving diffraction grating in the AOM-crystal is given by Θ_B. RF is short for the radio frequency source of the transducer. b) Relative intensity response of the AOM to a signals of different powers. The figure depicts an average of multiple measurements, normalized to the corresponding maximum intensity. This ensures the independence from laser intensity drifts. c) AOM step response versus time. The radio signal is switched on instantly at $t = 0$ (blue), and the output of the AOM is measured with a fast photo diode (red). The dead time of the AOM is indicated by t_1, whereas t_2 denotes the time until the steady state value of of the intensity is reached (rise time). The data is fitted with an error function (red). d) Gaussian beam profile calculated from the fitted error function.

the light fields, which adds further versatility to the transport operation.

In this chapter I will only go over the basic principles of polarization synthesis and phase manipulation, the detailed setup will be introduced in chapter 4.1.

1.3.1 Steering phase and amplitude of optical lattices

The phase and amplitude control of the optical lattice is achieved with acousto-optical modulators (AOMs). A detailed description of the working principle can be found in [33]. The AOM is driven by a radio signal of a digital vector generator at around 80 MHz, which is amplified to have a maximum power of 1 W, the saturation intensity of the AOM[1]. A schematic illustration is shown in figure 1.4 a. The working principle of the AOM is based around a piezo element inducing vibrations in a Tellurium-Dioxide crystal at the frequency of the driving radio signal. These vibrations will travel as phonons through the crystal at the material specific sound velocity, which is in this case $v_{\text{sound}} = 4.2\,\text{mm}/\mu\text{s}$. They produce a periodic modulation of the index of refraction, on which the phase of the radio signal is imprinted. As on any grating, the incident light can be reflected into one of the refraction orders for this specific wavelength. This can be understood by viewing the process as a phonon-photon interaction. If we denote the momentum

[1] Crystal Technologies AOMO 3080-122 [34]

of the incoming photon $\vec{k}_0$ and the one of the phonon $\vec{k}_{\text{phonon}}$ with

$$k_0 = \frac{2\pi\nu_0}{c} \qquad \text{and} \qquad k_{\text{phonon}} = \frac{2\pi\nu_{\text{radio}}}{v_{\text{sound}}}, \tag{1.12}$$

where $c = c_0 n$ is the speed of light in the crystal and ν is the respective frequency. Due to the law of momentum conservation the momentum of the photon after absorbing a phonon amounts to be

$$\vec{k}_1 = \vec{k}_0 + \vec{k}_{\text{phonon}}. \tag{1.13}$$

From energy conservation and equations 1.12 we infer that the light frequency is shifted by the phonon frequency, and that the phase of the acoustic wave is imprinted to the light wave:

$$\nu_1 = \nu_0 + \nu_{\text{radio}}. \tag{1.14}$$

In the complete setup, each polarization component is phase and amplitude controlled by an independent AOM. By modulating all lattice beams with a well defined phase, the relative phase between each pair can be controlled precisely. This approach however, demands a separation of the two components over a large portion of the beam path. Fluctuations between the two paths give rise to relative phase differences between the two polarization components, what might eventually heat the atoms. To prevent this effect, the phase is measured directly in front of the lattice position, and a feedback loop applies corrections to the radio signal to counteract phase and amplitude fluctuations,

Since the AOM will play an important role in the feedback loops for intensity and phase control, it is important to characterize the response function to a given input. The diffracted light power is in general not proportional to the input RF power. However, by limiting the radio frequency power to a certain range, we can operate in a regime where the refraction efficiency is monotonically increasing. The actual intensity response is plotted for one exemplary model in figure 1.4 b). By taking multiple measurements and normalizing the output to the maximum output power, the dependence on the input light intensity can be suppressed. The measurements show, that, while showing manageable nonlinear behavior especially in regions of lower/higher power, the response is time invariant and reproducible. This is important if we want to analytically treat the system later in section 3.1.2.

Figure 1.4 c shows the response function of the AOM to a signal applied at $t = 0$. The slope of the rise is defined by the Gaussian beam profile of the laser beam and the phonon velocity inside the crystal. The sound wave travels perpendicular to the light beam. As it crosses the Gaussian beam, the output intensity curve follows the error function. The delay until the rise begins at t_1 is defined by the distance of the beam path to the piezo oscillator. By fitting the response with an error function we can extract the two characteristic times t_1 and t_2. The dead time is defined as the time until the output reaches 1 % of its final value and amounts to $t_1 = 257\,\text{ns}$. The rise time is defined by the 99 % mark, and is given by $t_2 = 545\,\text{ns}$. From the fitted function and the sound velocity $v_{\text{sound}} = 4.2\,\text{mm/µs}$ we can calculate the Gaussian beam profile, shown in figure 1.4 d. This yields directly the beam diameter $d = 1.01(2)\,\text{mm}$ from the $1/e^2$-values of the Gaussian. This value is – when taking the possible divergence of a Gaussian beam into account – in good agreement with the experimental setup, where the beam is coming from a collimator[2] with a collimation diameter of $d' = 0.9\,\text{mm}$.

The characteristic times t_1 and t_2 in particular are critical properties of our setup, as the

[2] Schäfter & Kirchhoff M5 fiber coupler [35]

delay they impose to the response speed set an upper limit to the bandwidth of our system. The given time values represent the already optimized setup of this exemplary AOM model, where they have been minimized by adjusting the beam path. For the complete experimental setup, we use five AOMs in total, the response of which does not differ significantly.

1.3.2 Effect of phase noise on the optical lattice

Assuming a perfectly stable harmonic potential – as descried in section 1.1 – the lifetime of atoms in a far off-resonant dipole trap is usually limited by spontaneous processes to tens of seconds [36]. However, the lifetime can by drastically reduced by the motional excitations of the atom due to position-fluctuations of the optical lattice, caused by phase instabilities of the AOM driver. Further effects which disturb the stable operation of the lattice are intensity fluctuations and collisions with the background gas. However, these effects are small compared to the phase noise induced heating [28].

The phase of the intensity pattern and the corresponding position of atoms is given by equation 1.6. Following the calculations in [37, 36, 38], the heating rate for a one dimensional trapping potential caused by amplitude and phase fluctuations can be derived. The heating rate for a tree-dimensional confinement can be approximated by the sum of one-dimensional heating rates along each lattice dimension.

Heating due to intensity noise

We can describe the confinement of the optical lattice as a harmonic potential, which yields the Hamiltonian

$$H = \frac{p^2}{2m_{\mathrm{Cs}}} + \frac{1}{2} m_{\mathrm{Cs}} \omega_{\mathrm{tr}}^2 x^2, \tag{1.15}$$

where p and m_{Cs} are the momentum and the mass of the atom, and ω_{tr} is the trap frequencies defined in references 1.1. The trap depth fluctuations ϵ_x caused by the intensity noise introduce a perturbation term according to [38], such that

$$H(t) = H + H'(t), \text{ with } H'(t) = \frac{1}{2} \epsilon_x \omega_{\mathrm{tr}} x^2. \tag{1.16}$$

If we denote the initial vibrational state in the atom as $|n\rangle$, the average transition rate to a state $|m \neq n\rangle$ in a time interval T is given by Fermi's golden rule:

$$R_{m \leftarrow n} \equiv \frac{1}{T} \left| \frac{-i}{\hbar} \int_0^T dt' H'_{mn}(t') e^{i\omega_{mn} t'} \right|, \tag{1.17}$$

where ω_{mn} denotes the frequency difference between two motional energy states m and n – which is in our case equivalent to the trap frequencies ω_{tr}. The derivations in reference [38] give rise to an exponential increase of the average energy

$$\langle \dot{E} \rangle = \Gamma_x \langle E \rangle = \pi^2 \nu_{\mathrm{tr}}^2 S_a(2\nu_{\mathrm{tr}}) \langle E \rangle, \tag{1.18}$$

with the one dimensional heating rate Γ_x and the trap oscillation frequency $\nu_{\mathrm{tr}} = \omega_{\mathrm{tr}}/2\pi$ in Hertz. $S_a(f)$ is the one-sided power spectral density of the fractional intensity noise (see sec. 3.2.2).

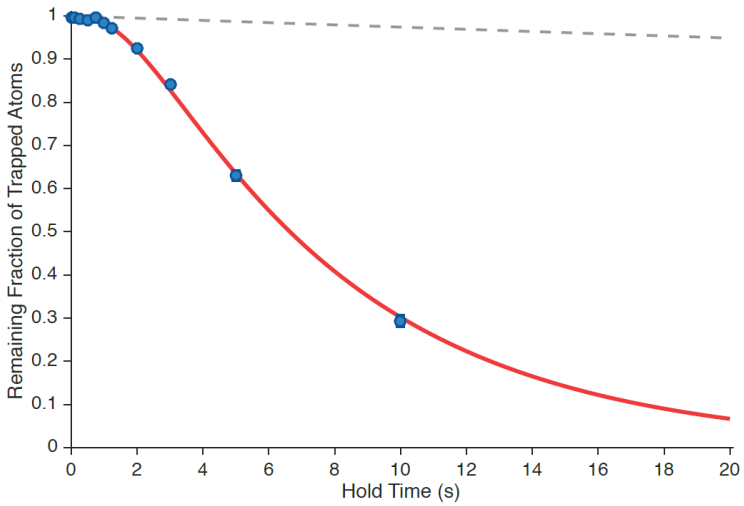

Figure 1.5: Storage time of atoms trapped in a (one-dimensional) optical lattice. The blue dots represent measured data, while the red line is a numerically simulated model using the Fokker-Planck equation to estimate the heating effect of phase noise (see Robens [14]). The grey dashed line shows the atom loss caused purely due to background collisions. The measurement and figure are originally published in Robens [14].

Heating due to phase noise

Fluctuations of the phase introduce a position jitter to the trapping potential, such that the Hamiltonian given by equation 1.15 of the system needs to be changed to

$$H(t) = \frac{p^2}{2m_{\mathrm{Cs}}} + \frac{1}{2} m_{\mathrm{Cs}} \omega_{\mathrm{tr}}^2 [x + \Delta x]^2, \tag{1.19}$$

where Δx is related to the phase noise through equations 1.6. According to [38], the procedure described above yields an average energy increase of

$$\langle \dot{E} \rangle = \frac{\pi}{2} m_{\mathrm{Cs}} \omega_{\mathrm{tr}}^4 S_x(\omega_{\mathrm{tr}}), \tag{1.20}$$

where $S_x(f)$ is the one-sided power spectrum of position fluctuations, related to the phase fluctuations $S_\phi(f)$ through equation 1.6 [39] (see also section 3.2.3).

To conclude, intensity as well as phase fluctuations of the lattice potentials induce heating of the atoms, which makes it necessary to stabilize both parameters. In previous works in our group it has been shown that the phase noise in particular is limiting the lifetime of atoms trapped in the optical lattice [14, 28].

Figure 1.5 shows the survival of atoms in a one dimensional lattice, once limited by phase noise influence and once only limited by background gas collisions [14]. The data shows clearly the reduced lifetime in the case of non-zero phase fluctuations compared to the case where phase noise is not present.

To calculate the heating rate of the two-dimensional lattice quantitatively from the spectral densities, the representation as two one-dimensional confinements is not sufficient. For this case, one would have to follow the derivations in [40, supplementary material], which is however out

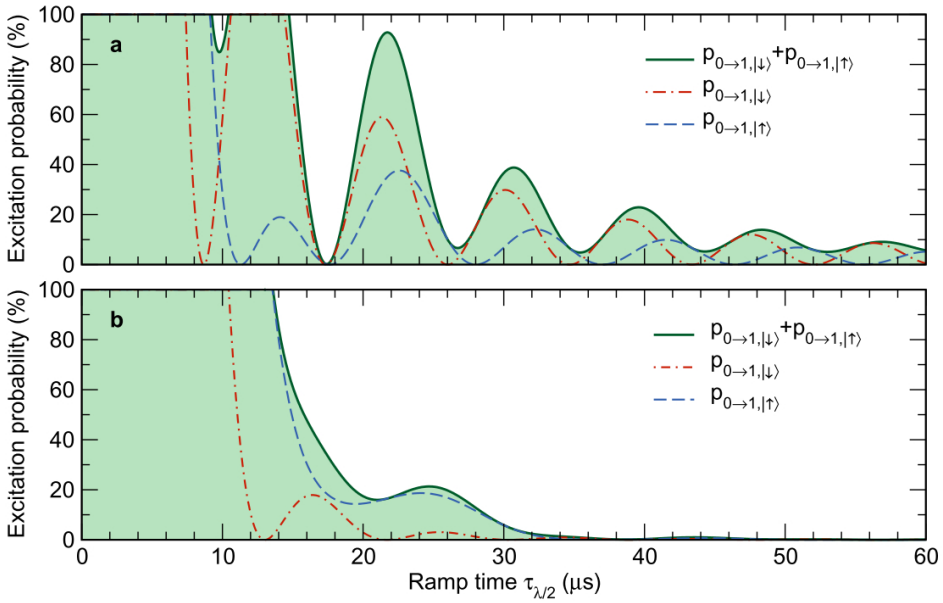

Figure 1.6: Probability to excite an atom trapped in a one-dimensional lattice from the axial ground state to the first vibrational excited state, when shifting the position of the lattice. The excitation probability is plotted against the transport ramp duration $\tau_{\lambda/2}$ for a linear shift operation (a) and for a cosinusoidal shift operation (b). the red dashed lines represent the excitation probability of the $|\downarrow\rangle$ state, the blues dashed line the $|\downarrow\rangle$, respectively. The sum of both is plotted as a green, solid line. This figure was originally published in [26].

of the scope of this thesis. Nevertheless, the calculations laid out in this section motivate the installation of a noise suppressing stabilization for both phase and intensity.

1.3.3 Effect of limited lattice bandwidth

One important property of the phase and amplitude stabilization setup is the control bandwidth. This parameter defines how fast deterministic phase changes can be applied, and therefore how many position shifts can be executed in a given time. Another parameter affected by the bandwidth is the motional state, i.e. the vibrational quantum number, of atoms trapped in the lattice. In the future, the atoms will be cooled to the vibrational ground state, both to ensure spin coherence and reduce hopping between lattice sites. Translations of the lattice which are non-adiabatic will increase the vibrational state of the atoms, and therefore destroy spin coherences. In Karski [26, chapter 4.4.3], the excitation from the motional ground state when applying linear and cosinusoidal transport ramps of different velocities is calculated. The findings are plotted in figure 1.6. The results are calculated assuming a one-dimensional lattice, but show nevertheless the importance of the control bandwidth. The excitation propability shows frequent minima in the case of a linear transport ramp. The fastest transport operation can be achieved with a ∼18 µs linear transport. For longer durations, the cosinusoidal transport ramp shows little excitations.

These transport speeds can still improved by employing optimal control theory. This concept relies on a phase ramp specially tailored to minimize transport excitations, and reaches transport durations as low as 8 µs [14, chapter 3.4.2]. This however demands a control setup which can

execute the phase ramps fast enough so that the optimal control ramp can be achieved.

The most limiting factor is in our case the delay time caused by the AOM response and the analog to digital conversions of the digital lock system. Fortunately, we are able to compensate this effect by a feedforward extension of the control loop. In the next chapter, I will introduce the digital vector generator on which the phase and amplitude control of the lattice is realized.

CHAPTER 2

A FPGA-based vector generator

In the last chapter we discussed the working principle of the two-dimensional state dependent transport scheme and established the necessity of precise phase and amplitude control. A detailed description of the analog stabilization setup implemented in the one-dimensional state-dependent transport experiment can be found in [14, 41]. In the work presented in this thesis, the entire control system is realized on a digital platform. The platform used to implement this digital control system is a versatile vector generator based on a field programmable gate array (Signadyne AIO-H3336F [42]). The FPGA enables the implementation of phase and amplitude control loops utilizing the on board digital signal processing capabilities.

This chapter will give aa brief overview of the digital vector generator module, and classify its phase noise performance in relation to currently employed vector generator systems.

Why digital control?

Digital control systems are gaining more and more in popularity. There are several advantages of digital systems over analog ones, for instance: [43]:

- **Accuracy.** Digital signals are represented in terms of zeros and ones, with a resolution of 16 bit in this case. This results in a relatively small error when compared to analog systems, where noise and power supply drifts are always present.

- **Reduced implementation errors.** The errors resulting from digital operations such as multiplication or addition are negligible compared to the typical variations of resistors and capacitors from the nominal design values.

- **Flexibility.** The modification of a state of the art analog controller involves a considerable amount of effort. Digital systems on the other hand can be reconfigured on a daily basis to implement new designs and signal processing modifications. This is convenient if one aims to optimize the behavior of a system.

- **Speed.** The speed of digital processing hardware has increased steadily since the 1980s. Todays digital control hardware is even without introducing controller modifications comparable to the state of the art analog equivalents (see section 3.2.2). The possibility to implement modifications tailored to the system specifications allows for even faster control, independent from the feedback bandwidth.

2.1 Introduction to the hardware

2.1.1 Hardware Overview

The main features of the Signadyne modules are the four vector-outputs, featuring an arbitrary waveform generator (AWG) for phase and amplitude modulation purposes. The output ports are capable of generating a low noise signal in a frequency range of 0–200 MHz. This signal will be used to drive the AOMs modulating the phase and amplitude of the optical lattice beams.

The output ports are paired with eight analog input ports, which are used to monitor the feedback signal in order to stabilize the phase and amplitude of the lattice beam. Input and output ports are combined on a FPGA (Xilinx Kintex-7 325T). The chip is programmable with a graphical user interface provided by Signadyne specifically for this purpose. The data structure located on the FPGA can be altered and extended to change the functionality of input/output ports at will. There is also the option to design and implement user generated intellectual properties (IPs) either with the program itself or with an external software.

Each of the FPGA modules is connected to a 10 MHz reference signal from an atomic clock, ensuring time synchronization between all employed devices. To start an experimental sequence, the devices receive a trigger signal from the main control unit[1], further ensuring synchronization. The modules are controlled via a PXIe connection to the main laboratory computer, yielding full control over the operation of the module.

2.1.2 Field programmable gate arrays

Field programmable gate arrays are silicon-based chips that feature a modular structure of digital gate operations. In contrast to application specific integrated circuits (ASICs), the logic layout of FPGAs can be reprogrammed. This fact makes FPGAs highly efficient for the computation of parallel tasks, as the structure of the chip can be designed specifically tailored for the purpose at hand. Therefore, the execution of the computation in parallel takes in most cases only one clock cycle. This is in contrast to common processors, where logic operations are sequentially executed by chaining one dimensional computations over multiple clock cycles.

The firmware design for the FPGA structure is done within a software developed by Signadyne specifically for the purpose of the modification of the vector generator modules, and reduces the – commonly complex – hardware coding to a graphical user interface. The simplified schematics shown in the following to illustrate the data structure on the FPGA are designed closely to the graphical interface, however for simplicity I reduced the information and data lines to exemplary ones and neglected the (for the section topic) unnecessary connections. The Signadyne software is able to compile the schematics into FPGA firmware files that can be loaded by the vector generator modules. The time it takes to compile a new firmware is even with cloud compilation in the order of two to three hours.

2.1.3 Output ports and modulation

The Signadyne output channels consist of a function generator unit, a modulation/gain unit and an arbitrary waveform generator. A schematic overview of the output port structure is illustrated in figure 2.1. The function generator, as well as the modulation/gain unit, are controlled via the PXIe connection, which provides static parameter words such as the center

[1] ADwin Pro II

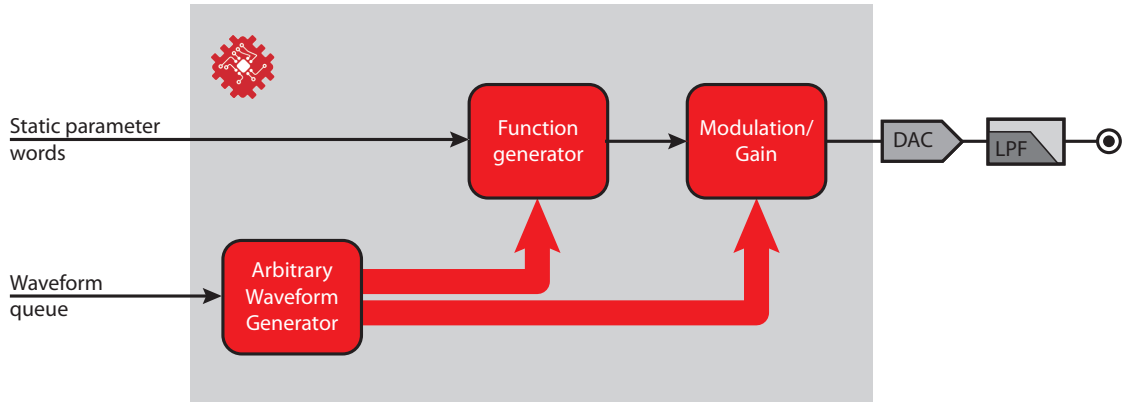

Figure 2.1: Signadyne AWG output functional block diagram. The gray box is an indication which processes are executed on the FPGA unit. Black arrows represent standard data connections. Red arrows indicate the data streams which are programmed by the experiment controller.

frequency and phase of the signal. Based on these values, the function generator produces a data stream that is fed to the modulation/gain stage. The modulation/gain unit has similar input parameters as the function generator, in this case for amplitude and offset of the signal. The data received from the function generator is amplified with a voltage specified with the amplitude word, and sent to the output. The output signal then has the form

$$U_{\text{out}}(t) = A\cos(2\pi f_{\text{c}} + \phi_{\text{c}}) + B, \tag{2.1}$$

where A is the amplitude voltage, f_c is the carrier frequency, ϕ_c is the carrier phase and B is the offset voltage.

Both the frequency generator and the modulation/gain unit also receive inputs from an arbitrary waveform generator (AWG), and use the provided data stream for modulation of frequency, phase, amplitude or offset. The data received is stored in a range of [-1:1], normalized to 16 bit, and is rescaled according to the modulation gain that is programmed into the respective module. Only phase or frequency can be modulated by the function generator at the same time, while the modulation/gain unit can either modulate amplitude or offset. For example, the output with active phase and amplitude modulation would read

$$U_{\text{out}}(t) = (A + G_A \cdot \text{AWG}_1(t))\cos(2\pi f_{\text{c}} + \phi_{\text{c}} + G_\phi \cdot \text{AWG}_2(t)) + B. \tag{2.2}$$

Here G_{A} and G_ϕ are the modulation gains and $\text{AWG}_1(t)$ and $\text{AWG}_2(t)$ are the signal streams provided by the AWG.
The data lines connecting the AWG to the receiving modules are multiplexed, enabling a 500 MSPs (Mega samples per second) modulation. To prevent excessive usage of memory, the AWGs can be programmed with a versatile queuing system to program a sequence of waveforms that can be cycled, reused and scaled down in terms of sampling frequency if needed. To utilize this in a user-friendly manner and to incorporate it into the experimental operation a data adapter was set up to program sequences with efficient memory usage and high flexibility. This system will be introduced in the next section, where I will give a detailed description of the

AWG queue.

2.1.4 Arbitrary waveform generators for modulation

In section 2.1.3 we first mentioned the arbitrary waveform generators (AWG) located on the FPGA-chip. The AWGs are used to supply data streams for phase and amplitude modulation with a high time precision (up to 500 MSPs). They are of crucial importance to the experiment, as they will be used to steer the phase and amplitude of the optical lattice. Figure 2.1 shows the AWG data streams as red arrows, to emphasize that the data carried by this lines steers the operation of the module precisely. Each of the four output channels of the Signadyne module features an AWG capable of providing a two-dimensional data stream with 2x16 bit resolution. Originally, the data is routed to the modulation inputs at the frequency generator and the modulation/gain block (see figure 2.1). It can however be redistributed on the FPGA and serve numerous purposes.

The data sequence provided by the AWGs is produced by seamlessly concatenating individual waveforms in the RAM-memory. This however demands a complicated queuing effort, including the specification of the waveform, sample time, delay, number of repetitions and the trigger mode. I have programmed a queuing algorithm to reduce the complexity of the sequence generation for the end-user. The device is included as an object into the experiment controller software which was set up by Stefan Brakhane. The purely Matlab based environment includes a data adapter for the Signadyne waveform queuing system, which automates the choice of queue parameters to a great amount. The operation of this adapter are laid out in the following section.

Programming the AWG queue

The experimental execution is designed such that every involved device is pre-programmed by a sequential stream of parameter values. These sequences are then simultaneously executed to steer the experimental apparatus. To integrate the FPGA-module in the Matlab based experiment controller, the AWG queue programming is to a high extend automated to reduce the complexity of programming an experimental sequence.

The AWG queue creates a data stream by aligning predefined waveforms loaded to the on-board RAM. This enables us to program the setpoint sequence for a complete experimental operation. The data adapter programmed for this purpose implements a queuing algorithm I wrote to reduce overhead and simplify the operation. Tasks undertaken by this adapter are:

Re-usage of Waveforms: The AWG queue is based on an ID system, allowing to execute waveforms that are stored in the RAM of the module to be re-used and cycled virtually infinitely. This is of great importance to the operation, since the length of the sequence is limited by the storage capability for data samples. During the sequence compilation, the adapter automatically compares new waveforms to already existing ones and stores only one iteration of duplicates, which highly reduces the memory usage.

Calculation of sampling rate: The sampling rate of any given waveform is automatically calculated from the duration of the ramp. If it is not specified how precise the waveform should be sampled, the adapter opts for a sampling rate which is dependent of the length of the ramp. This reduces memory usage further, as slower ramps are more coarsely sampled.

Managing idle times: Idle times are a further factor which drains the data-memory of the AWGs. The experimental sequence contains multiple idle times which require the majority of devices to stand by for durations in the order of milliseconds to a few seconds – e.g. for MOT

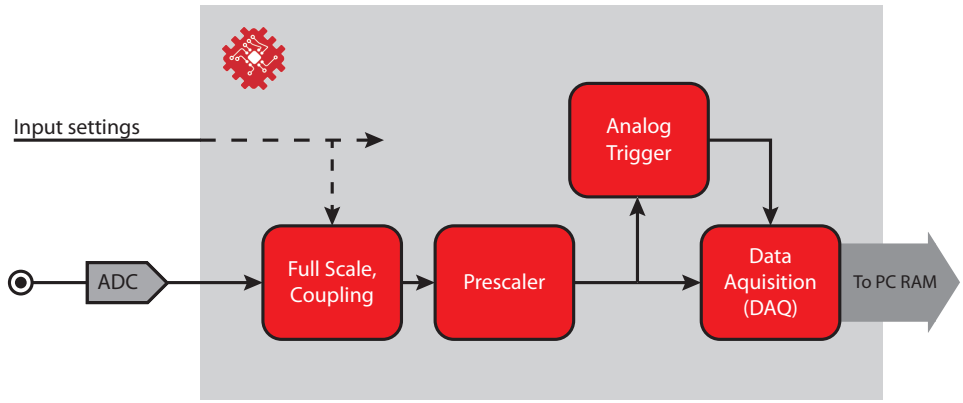

Figure 2.2: Signadyne Digitizer input functional block diagram. Shown is one channel, all channels have an identical structure. The grey box is an indication which processes are executed on the FPGA unit. The input settings are applied via the PXIe connection. for simplicity, the connections to some of the units are neglected, although all of them have a configuration parameter provided by this line. The input can be configured in terms of Full Scale and coupling. The data provided by the ADC can be prescaled, so that only one out of n samples is fed to the data line. Each line is monitored by an analog trigger block, which can be used to time various operations on the FPGA depending on the input voltage. Finally, the data from the input port can be recorded by the DAQ module, which can be used to read data and send it to the main computer.

preparation. Producing constant output over such times is unfeasible for AWGs, since the delays between waveforms is limited to a few tens of micro-seconds. For this purpose, the data adapter has the ability to queue a number of waveforms with minimal sampling points. To cover the idle durations, these waveforms are queued multiple times at a low sampling rate. This enables idle times of durations from 10 ns up to minutes, without affecting the data usage.

Managing trigger: The AWG queue is able to store a specific trigger for any waveform in the queue, if necessary. The corresponding waveform will be delayed until the specified trigger is received. To simplify the operation of this feature, the adapter-object scans the trigger line – which is also existent in the digital sequence in Matlab – and compares it to its own waveform queue. It then applies the appropriate triggers to the waveforms of the corresponding time, such that the module automatically expects a trigger at the scheduled times of the experimental execution.

The AWGs of the FPGA-modules are an important part of the control loops, as they provide the precisely planned setpoint time trace for the controllers. The FPGA structure enables the re-routing of the data stream to serve any purpose, which is put to use in the advanced control scheme introduced in 3.3.2.

2.1.5 Input ports and data acquisition

The input ports of the FPGA-module are used to provide the feedback data for the control loops discussed in chapter 3. The data acquisition and input port structure is illustrated in 2.2. The analog data is converted to a digital data stream by an analog to digital converter (ADC). The full scaling of the input – defining the maximum of the analog input – as well as the impedance matching can be programmed for each channel independently. This enables us to automatically

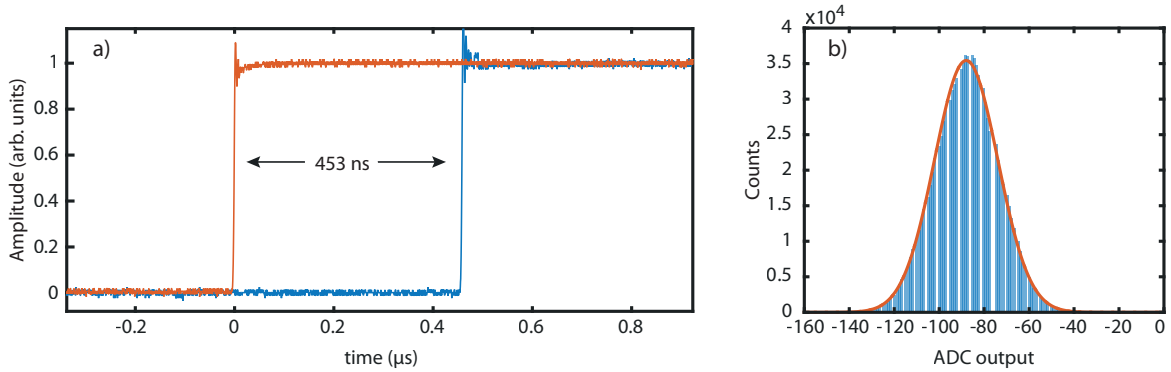

Figure 2.3: Input/Output characterization measurements. a) Input/Output delay of the FPGA module with minimal computation. One output signal(blue) is connected to an input channel and used as a trigger. The delay to the resulting output is measured to be $T_D = 453\,\text{ns}$. b) Distribution of output values of the DAC. The output of the ADC is recorded for $200 \times 5000 = 10^6$ samples. The mean μ and standard deviation σ of the data is used to plot the corresponding gaussian distribution of the data (red)

adjust the ADC conversion to drifts of the lock signal amplitudes. Besides from providing continuous feedback signals for the controllers, the modules can also record data and send them to the main computer over the PXIe connection. Recording the data words is possible with the data acquisition units (DAQs) on the FPGA. The data is first stored on the on board memory, and can be loaded from the main computer. To start the data acquisition, the DAQs can be triggered on a selection of trigger signals, either provided by the analog triggers or by digital signals provided by the logic structure of the FPGA design. The analog triggers in particular are useful to monitor e.g. the error signals of the feedback loops at specific points in the experimental sequence by re-routing the setpoint streams to the trigger blocks. This functionality can be used to automatically tune the control parameters, but is not fully implemented yet. Nevertheless, in the future the controller tuning can be automated to function at the press of a button.
The number of data words that can be recorded at once is in principle limited by the 2 GB of on board memory. A continuous monitoring via the main computer is not possible, as the data rate produced by the DAQs is more than the PXIe connection can support.

2.2 Hardware characterization

2.2.1 Data resolution and input/output delay

In order to characterize the time delay from input to output of the system, the FPGA is loaded with a minimal firmware connecting one of the input channels internally to modulate one of the output channels. A step signal applied to this channel will result in a step signal on the output, delayed by the internal operations of the digital module and the processing time of the DACs and ADCs. The resulting data is displayed in figure 2.2.1 a. The resulting input/output delay amounts to T_{IO} =453 ns.

Figure 2.2.1 b shows the distribution of the data measured by the ADC. The measurement is taken by grounding one of the input channels with a 50 Ω resistance and reading the corresponding ADC data output. Taking the standard deviation of the data yields

$$\sigma_{\text{ADC}} = 29.12, \tag{2.3}$$

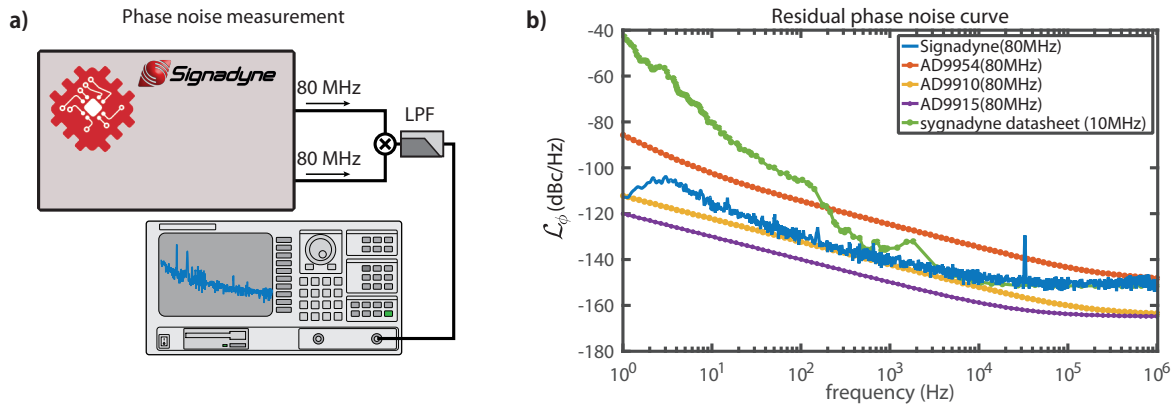

Figure 2.4: Phase noise measurement setup and data comparison of different systems. a) Schematic of the phase noise measurement technique. Two signal channels of the same center frequency are mixed by a phase discriminator and the difference frequency is isolated by a low pass filter. This signal is fed to a spectrum analyzer to extract the spectral density of the phase signal. b) Phase spectral density with respect to the carrier signal of various DDS systems. The Signadyne module discussed in this chapter is compared against the data sheet specifications of three DDS chips at 80 MHz, and a measurement provided by the company at 10 MHz. For the ladder case, the increased noise at lower frequencies can be explained by the lower center frequency, as is laid out in [47]. This measurement was performed by Gautam Ramola

which corresponds to roughly a spread of five bits. This reduces the effective resolution of the ADCs to

$$N_{\text{eff}} = 11\,\text{bits}. \tag{2.4}$$

The Signadyne data sheet specifies a nominal voltage resolution of the inputs of $N_{\text{spec}} = 14$ bits. The discrepancy here might originate from the nominal value being achieved under optimal conditions which might not be reproducible under the layout constraint of the circuit boards [44]. Nevertheless this will pose a limit on the amplitude noise suppression.

2.3 Phase noise characterization

The phase noise of the output signal is an important property of the vector generator module, as discussed in section 1.3.2. The presented system is working in the discrete time domain and generates sinusoidal signals by direct direct digital synthesis (DDS) [45]. The working principle of DDS waveform generation is based on a fixed phase accumulation per sample time and a mapping of said phase to a predefined amplitude. Phase noise is caused by the finite resolution of phase-amplitude mapping and also by the jitter of the reference clock frequency [46]. This leads to variations in the continuous time sine-wave that is produced by the low pass filtering of the digital signal.

In section 2.1 we have defined the output of the Signadyne vector generator module as

$$U_{\text{out}}(t) = A\cos(2\pi f_{\text{c}} t + \phi_{\text{c}}) + B. \tag{2.5}$$

Including phase noise in this equation, the ideally static phase ϕ_{c} becomes time dependent, with

$$\phi_{\text{c}}(t) = \phi_{\text{c}} + \delta\phi(t). \tag{2.6}$$

Oscillatory deviations like the phase noise are commonly described in the frequency domain, by the spectral density $S_x(f)$ [39]. The spectral density describes the power fluctuations in a frequency span of one hertz. $S_x(f)$ can be measured by most commercial spectrum analyzers in units of voltage squared per hertz. By applying a well defined measurement method $S_x(f)$ can be converted to the desired single sideband phase fluctuations. To measure the phase fluctuations around a center frequency f_c, the signal, given by 2.6, is mixed with a signal with preferably lower or equal phase noise. In first order approximation the output signal of the mixer is given by a multiplication of the two input signals. In this case the phase fluctuations are measured by two channels of the Signadyne module, so that the mixer output yields

$$U_m(t) = \alpha A^2 \sin(2\pi f_c + \phi_1(t)) \sin(2\pi f_c + \phi_2(t)) = \frac{\alpha}{2} A^2 (\cos(\phi_1(t) - \phi_2(t)) + \cos(4\pi f_c t + \phi_1(t) + \phi_2(t))), \tag{2.7}$$

where α is a proportional constant of the mixer and we assumed a vanishing offset $B = 0$, as well as a common amplitude A and carrier frequency f_c. The respective phases of the two signals are given as $\phi_1(t)$ and $\phi_2(t)$. By applying a low pass filter we can suppress the fast oscillating second term in equation 2.7, so that we are left with a cosine-term which has as argument only the difference of the phases of the two signals:

$$U_m(t) = \frac{\alpha}{2} A^2 \cos(\phi_1(t) - \phi_2(t)). \tag{2.8}$$

By tuning the two output channels with a difference of 90° from one another, the small angle approximation can be applied and for small changes in the phase the mixer output gives a value directly proportional to the phase fluctuations

$$U_m(t) = \frac{\alpha}{2} A^2 (\delta\phi_1(t) - \delta\phi_2(t)) = \frac{\alpha}{2} A^2 \Delta\phi(t). \tag{2.9}$$

According to [48], since both $\delta\phi_1(t)$ and $\delta\phi_2(t)$ are random processes, the computation is only viable for statistical quantities such as the mean-squared voltage

$$\overline{U_m^2(t)} = \left[\frac{\alpha}{2} A^2\right]^2 \overline{\Delta\phi^2(t)}. \tag{2.10}$$

However, if we substitute the random fluctuations $\Delta\phi(t)$ by a well defined phase modulation $\phi(t)$, the mixer constant can be measured as

$$K_\phi \equiv \frac{\alpha}{2} A^2 = \frac{U_m(t)}{\phi(t)} \quad V/rad, \tag{2.11}$$

if a mixer type phase discriminator is used. To measure the mixer constant K_ϕ, a setup similar to the one shown in figure 2.4 a is used. The spectrum analyzer is, for this purpose, substituted by an oscilloscope or a multimeter, to measure the voltage $U_m(t)$. The phase $\phi(t)$ can be digitally changed directly at one of the outputs of the Signadyne module, by changing the corresponding phase-word. From this data the voltage per phase increment can be measured and used to convert the power spectral density $S_x(f)$ – measured by the spectrum analyzer as illustrated in figure 2.4 a – to double-sided phase spectral density $S_\phi(f)$. The IEEE definition of the phase

phase noise is

$$\mathcal{L}_\phi(f) = \frac{\text{power density in one modulation sideband, per Hz}}{\text{total signal power}} \tag{2.12}$$

and is usually expressed in decibels(dB), as $10\log_{10}(\mathcal{L}_\phi(f))$ [39]. It can be related to the phase spectral density $S_\phi(f)$ by

$$\mathcal{L}_\phi(f) \equiv \frac{S_\phi(f)}{2}. \tag{2.13}$$

The unit degree squared per Hz is for most measurements more intuitive, but to compare the phase noise to ones of other systems the $\mathcal{L}_\phi(f)$ definition is better suited. Figure 2.4 b show the phase noise $\mathcal{L}_\phi(f)$ with respect to carrier for the new Signadyne vector generator as well as other DDS chips commonly used as reference for phase stabilization. For instance in the one-dimensional quantum walk experiment of our group the phase lock reference is provided by the AD9954 DDS chip (red in figure 2.4). Recently, there has also been made an effort to design a DDS box interfaced with an FPGA which employed the more stable AD9915 chips (purple). Further details in this direction can be found in Ramola [49]. The Signadyne device (plotted in blue) can be classified as a compromise between the two systems, providing a wide range of well designed and flexible features while showing a moderate improvement in terms of phase noise compared to the AD9954 chip. All specifications shown are for a carrier frequency of 80 MHz, which is the driving frequency for the AOMs we employ to steer the optical lattice. The spectrum provided by Signadyne however is taken for a center frequency of 10 MHz, which explains the increased phase fluctuations in regions close to the carrier, since the effect of phase noise is more dominant at lower center frequencies [47, Chapter 5.5]. The increased phase noise of the Signadyne module when compared against the AD9915 DDS unit (about one order of magnitude in the region of the trap frequency) is a trade-off against the highly reduced development time that would be required to reach the level of integration between the DDS and the FPGA of the commercially bought vector generator by Signadyne. However, if the development of the in-house DDS signal generators is further pursued the reduction of phase noise would increase the life time of atoms in the lattice proportionally, as shown in Robens [14, Chapter 2.1.2].

CHAPTER 3

Digital feedback control of phase and amplitude

In the last chapter I gave an overview over the FPGA structure and how the different stages of the FPGA interplay with each other. This chapter will utilize the basis of the last and cover my work in terms of development and implementation of the phase and amplitude control loops. I will first introduce the fundamentals of control theory, which are later used to analyze and characterize the control loops.

Both phase and intensity control loops are realized using a PID(proportional, integral, derivative) controller. This type of controller is commonly used in scientific applications and makes up the base level of 95 % of control loops in modern process control [50]. The second part of this chapter describes the optical setup and the characterization of the control systems. In the last sections of this chapter I will present an extension of the phase control loop to a feedforward control scheme, which compensates for the effect of dead time by means of internal model control. Without the limitation of this effect, the control bandwidth for deterministic transport in the optical lattice can be drastically increased to be limited only by the inherent response time of the controlling hardware.

3.1 Control theory: feedback system design

The typical requirements for a feedback controller are to follow reference signals and recover the system from load disturbances and process variations [50]. The most commonly used feedback scheme is the PID-controller, which will be introduced in the first section of this chapter. Since the fast response to user inputs is of great importance, this controller will be extended by a feedforward application to take care of fast, deterministic output changes.

3.1.1 The PID-controller principle

The control action of a PID-controller can be described by [50]

$$u(t) = k_\mathrm{p} e(t) + k_\mathrm{i} \int_0^t e(\tau) d\tau + k_\mathrm{d} \frac{de(t)}{dt}, \tag{3.1}$$

where u is the control signal and $e = y_\mathrm{sp} - y$ is the control error. The control error is defined as the difference between the reference variable y_sp (commonly called the setpoint) set by the

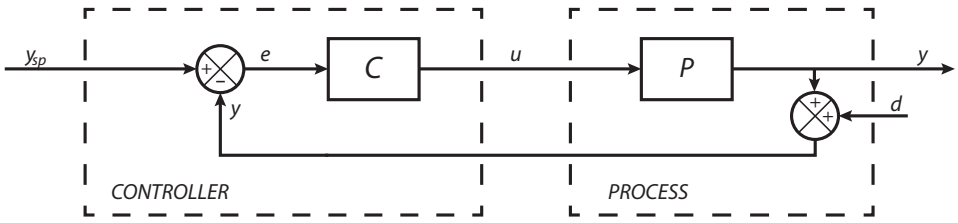

Figure 3.1: Block diagram of a feedback control loop. The user sets the setpoint y_{sp}, from which the error signal e is derived by subtracting the measured system value y. The controller C acts on the error signal e and produces a system input u to the process. Instabilities in the environment, the measurement and the process itself add disturbances d to the signal. The process reacts to the input according to its response function P. The resulting value y is fed back and subtracted from the setpoint value, which closes the loop.

user, and the measured process variable y. The controller parameters are the proportional gain $k_{\mathrm{p}} = K_{\mathrm{p}}$, the integral gain $k_{\mathrm{i}} = K_{\mathrm{p}}/T_{\mathrm{i}}$ and the derivative gain $k_{\mathrm{d}} = K_{\mathrm{p}}T_{\mathrm{d}}$, where the latter can also be defined with a universal gain constant K_{p} and their respective time constants T_{i} and T_{d}. In the end the control action for both configurations is equivalent, but one has to keep in mind how the individual controller has to be addressed.

The proportional action is the most intuitive part of the controller. It tries to immediately counteract deviations from the setpoint value, by applying a proportional correction in the opposite direction. This will decrease the error value at this instant, but a continuous compensation is not possible. Since the output depends only on the error value at the specific point in time, a pure P-controller will always result in a non-zero steady state error. Increasing the gain will reduce the initial error, but leads to oscillations after a certain critical point that depends on the bandwidth of the system. This issue can be resolved by adding the integral action. The I-part of the controller will increase its action as long as the error value is non-zero. However it lacks the quick reaction speed of the proportional controller. By combining the two, the reaction time as well as the steady state error can be optimized. The derivative action can be used as a prediction of the system behavior, if the derivative time constant is chosen correctly [50]. It counteracts rapid changes of the signal, dampening oscillations caused by e.g. overtuned P- and I-gains. Further insight of the process and controller interaction can be gained in the frequency domain through a Laplace transformation defined by equation 3.5.

3.1.2 Description in the frequency domain

Many systems in nature are difficult to describe in the time domain, as one has to solve numerous linear differential equations in order to find the solution. In the frequency domain it is more feasible to characterize and analytically describe systems, given they are linear and time invariant (commonly called LTI systems).
The Fourier transform is well suited to describe oscillatory functions in the frequency domain, since they are periodic in time. However, if the system requires in addition a dampening term– such as the discharge of a capacitor – a Fourier transform is no longer sufficient [51]. To describe such dampening or build up, the more general approach of the Laplace transform is better suited. The Laplace transform works similar to the Fourier transform, as it maps to a complex

valued number $s = i\omega + \rho$, extending the purely imaginary angular frequency $i\omega$ by a real valued attenuation ρ. The formal Laplace transformation of a given function $f(t)$ is therefore written as

$$\mathcal{L}\{f\}(s) = \int_0^t f(t)e^{-st}dt. \tag{3.2}$$

Here it is noteworthy that in contrast to the Fourier transform the integration is only carried out for $t \geq 0$, which are more relevant limits for the majority of physical measurements.
The transfer function of a system is defined by the Laplace transforms of the input relative to that of the output:

$$G(s) = \frac{Y(s)}{U(s)} = \frac{\mathcal{L}\{y\}}{\mathcal{L}\{u\}}, \tag{3.3}$$

where $U(s) = \mathcal{L}\{u\}$ is the Laplace transform of the input u of a linear system, and $Y(s) = \mathcal{L}\{y\}$ is the Laplace transform of the output y [52]. This holds under the assumption that all initial conditions are zero and the system is linear and time invariant. Most system transfer functions can be rewritten as a fraction

$$G(s) = \frac{n_{\mathrm{G}}(s)}{d_{\mathrm{G}}(s)}, \tag{3.4}$$

where n_{G} and d_{G} are polynomials in s. The roots of n_{G} and d_{G} are the so-called *zeros* and *poles* of the system, respectively. The poles in particular define the behavior of the system response to a given input, which is why the denominator $d_{\mathrm{G}}(s)$ is also called the characteristic equation of the system [53]. The order of the polynomial $d_{\mathrm{G}}(s)$ defines also the order of the respective system.

The treatment of the PID-control action is convenient in the Laplace space due to the transformation of derivatives and integrals: the n-th derivative corresponds to a factor of s^n; integrations, being the inverse derivatives, result therefore in factors of $1/s$. After the Laplace transformation the transfer function of the PID-controller C from equation 3.1 amounts to

$$C(s) = k_{\mathrm{p}} + \frac{k_{\mathrm{i}}}{s} + k_{\mathrm{d}}s. \tag{3.5}$$

To calculate the transfer function of complex networks, the convolution integral in the time domain transforms to a straightforward multiplication of the transfer function. The closed loop transfer function of the feedback loop illustrated in figure 3.1 can be derived to be

$$G(s) = \frac{C(s)P(s)}{1 + C(s)P(s)} = \frac{L(s)}{1 + L(s)}. \tag{3.6}$$

Here we already used the open loop transfer function $L(s) = C(s)P(s)$. The complexity of $G(s)$ depends strongly on the system P.

3.1.3 Description in the time domain: the step response

While the frequency domain is well suited to describe the behavior of LTI systems, it is only indirectly accessible through the time domain. To characterize the performance of a system in frequency space, the general procedure is to give a well defined input and monitor the resulting transient response in time domain, so that the frequency dependent behavior can be calculated. The most desirable input would be an impulse, as the corresponding Laplace transformation is given by the unitary constant, equally exciting all frequencies. Since a perfect impulse is not

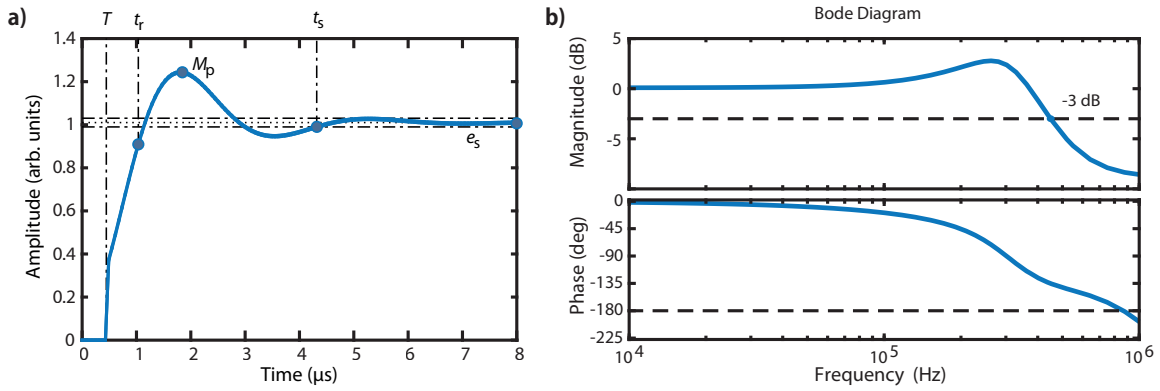

Figure 3.2: Exemplary time and frequency domain data of a model system. a) Transient response to a step input given at $t = 0$. Typical characteristic properties are indicated, such as the deadtime T, the rise time t_r, the peak magnitude M_p, the settling time t_s and the steady state error e_s. b) Bode plot derived from the model system. The dashed lines mark the -3 dB margin for the magnitude plot and the -180° margin in case of the phase angle plot.

easy to achieve in the real world, the next best choice is the Heaviside step function

$$\Theta(t), \text{ with } \mathcal{L}\{\Theta(t)\}(s) = \frac{1}{s}. \tag{3.7}$$

Figure 3.2 a shows an exemplary response to a step input given at $t = 0$. From the corresponding transfer function we can construct the bode plot by evaluating the closed loop transfer function $G(s)$ for purely imaginary frequencies $s = i\omega$. This way we assess the system behavior for purely sinusoidal inputs. An example Bode diagram corresponding to the transient response is shown in figure 3.2 b. The Bode diagram consists of two parts: [54, Chapter 7-2]: One is a plot of the logarithmic amplitude $20 \log |G(i\omega)|$ in decibel(dB). The other plot is of the argument $\arg [G(iw)]$ in degree or radian. Both quantities are plotted against the logarithmic frequency scale. From the bode plot several characteristics of the system can be extracted, such as the bandwidth and the stability margins. The bandwidth f_B of a system is defined as the -3 dB crossing of the magnitude plot. As for the Bode plot, there are several properties of the transient response which can be used as an indicator for the system performance [54, Chapter 5-3]:

- Dead time (T): The delay time it takes for the system to start reacting to a given input. dead time is one of the predominant limiting factor when it comes to control, hence there are numerous proposals on how to compensate its effect. We will later see that, in fact, in our system the dead time imposes the biggest constrain on the bandwidth.

- Rise time (t_r): The rise time is usually defined as the time the response takes to rise to 100 % of the final value. The rise time is the characteristic of the system which is closely linked to the control bandwidth ω_B by the relation $t_r \simeq 1/\omega_B$.

- Maximum overshoot (M_p): The maximum overshoot is the maximum peak value of the response function compared to the final value. The amount of maximum overshoot is directly related to the stability of the system.

- Settling time (t_s): The settling time is defined as the time it takes for the system error to converge in the 2 % region around the set value. The settling time is the largest time

scale of the system. After the settling time, there are no remains of the input signal in the system value.

Estimating general controller tuning rules

To give a more physical connection to the control parameters, let us consider a system of second order. We will neglect the dead time for now, as it adds a lot of complexity to the system. The following calculations are based roughly on [55]. The controller is for this example estimated as a PI-controller, as the majority of the control action originates from the proportional and integral parts. This means we can use equation 3.5 with derivative gain $k_\mathrm{d} = 0$ as our controller approximation. For the process model we will use a simple first order approximation given by

$$P(s) = \frac{b}{s+a}.$$

In this case a and b are arbitrary process parameters. With these assumptions we can calculate the open loop transfer function

$$L(s) = C(s)P(s) = \frac{k_\mathrm{p} b s + k_\mathrm{i} b}{s(s+a)} = \frac{n_\mathrm{G}(s)}{d_\mathrm{G}(s)}. \tag{3.8}$$

The feedback loop is assumed to have the same structure as the one presented in figure 3.2. Therefore, the feedback transfer function is given by equation 3.6:

$$G(s) = \frac{C(s)P(s)}{1 + C(s)P(s)} = \frac{n_\mathrm{G}(s)}{d_\mathrm{G}(s) + n_\mathrm{G}(s)} \tag{3.9}$$

We can compare the closed loop transfer function of this model to the standard form of a second order system

$$\frac{\omega_0^2}{s^2 + 2\zeta\omega_0 s + \omega_0^2}, \tag{3.10}$$

and this way connect the characteristics of the transient response to the control gain parameters. Here, ζ is a dampening ratio and ω_0 is the undamped natural frequency of a standard second order system [54]. These quantities are directly linked to the transient response characteristics, as ω_0 is a measure for the overall speed of the response and ζ gives an indication of the general shape. It is notable that our model system is actually different from the one in equation 3.10 as it includes one zero. Nevertheless as the characteristic polynomials

$$d_\mathrm{G}(s) + n_\mathrm{G}(s) = s^2 + (k_\mathrm{p} b + a)s + k_\mathrm{i} b = s^2 + 2\zeta\omega_0 s + \omega_0^2 \tag{3.11}$$

are of the same order we can still draw connections to the tuning parameters of our system. By matching the coefficients in equation 3.11 we arrive at the relations

$$k_\mathrm{p} = \tfrac{2\zeta\omega_0 - a}{b}, \tag{3.12}$$

$$k_\mathrm{i} = \tfrac{\omega_0^2}{b}. \tag{3.13}$$

We can directly draw the conclusion that the integral gain has the highest influence on the reaction speed ω_0, while the overall shape can be influenced by tuning ζ using the proportional gain. In [54, Chapter 5-3] the transient response of a standard second order system is calculated

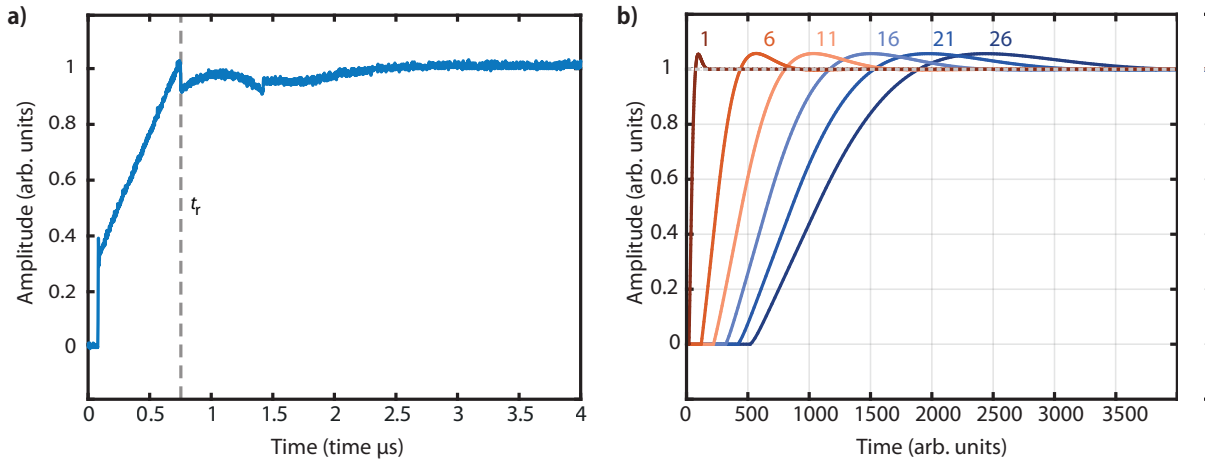

Figure 3.3: Dead time limitations on the response speed of a closed feedback loop. a) Step responses of an identical system with different values for the dead time T. the integer number above the respective responses is the dead time T of that system in the time scale of the simulation. b) Step response of a PI-controller acting on a process of pure dead time.

by convolving the unit step with the transfer function of the system. There are three cases for the shape of the transient response, out of which only one is of interest for us. For $\zeta \geq 1$ the system is called *overdamped*, and exhibits a slowly converging response. For $\zeta \to 0$ the system starts to become *underdamped* and the signal will show oscillations around the setpoint value. The fastest response and settling time can be achieved for damping ratios of $0.4 \leq \zeta \leq 0.8$. In this regime the oscillations caused by the overshoot are dampened below the 2 % threshold after roughly one oscillation period.

The dead time performance limit

The step response shown in figure 3.3 a is a good example for the behavior of a system governed by dead time. It is, in fact, the closed loop response of the digital controller (see sec. 3.2.1), where the process is provided by a cable connection from analog output to analog input. The main dead time limitation originates in this case from the input/output delay $T_{\mathrm{IO}} = 453\,\mathrm{ns}$ of the hardware we discussed in chapter 2.1.5.

The first part (until t_r) of the response function gives an intuitive picture of the control action for such a system. The curve of the transient response can be approximated in intervals on the dead time, since in the time immediately after the step it is the most dominant factor. The first initial rise is caused solely by the proportional action. Since the trigger is also affected by the output delay, the initial dead time cycle is only due to the computation time caused by the controller $T_{\mathrm{PID}} = 80\,\mathrm{ns}$ (see sec. 3.2.1). For the next time interval, the integral action is constantly increasing due to the fact that the error has been constant for one time interval $T = T_{\mathrm{PID}} + T_{\mathrm{IO}}$. The accumulation of this constant results in a linear rise of the control action. In the subsequent dead time intervals, the integrator includes the previous period into its action, such that the order increases by one. This is a considerable limitation to the reaction speed of the controller, as the integration gain is limited by the interval of first order. The fastest response can be achieved if the controller is tuned such that the output value is close to the setpoint after this initial period. We can roughly estimate the bandwidth ω_{b} and overshoot M_{p}

from the dead time and controller gain, by approximating the bandwidth as

$$\omega_\mathrm{b} \simeq \frac{1}{t_\mathrm{r}} \approx \frac{1}{T_\mathrm{IO} + 2T_\mathrm{PID}} \simeq 1.63\,\mathrm{MHz}. \tag{3.14}$$

The maximum overshoot can be estimated by assuming a unit step, and neglecting the additional rise caused by higher order dead time intervals. This imposes a lower boundary

$$M_\mathrm{p} \geq k_p + k_i \int_0^T e(t)dt = k_\mathrm{p} + k_\mathrm{i} T \tag{3.15}$$

for the gain parameters if we want the response overshoot to be within reasonable limits. Although this is only a rough estimation of the control system, it shows the inverse scaling of both the bandwidth and the integral gain with the dead time T, and therefore the limitation it imposes on the system. Figure 3.3 b shows the closed loop response to a step input at $t = 0$ of the model system used earlier in this section with different values of dead time T. The PI-controller has been tuned to achieve the same shape of the response for each system. The simulation again shows the rough dependency $t_\mathrm{r} \propto T$. While dead time in open loop control is compensated effortlessly by earlier execution of system inputs, this example goes to show that the system feedback control speed heavily decreases for larger dead time components.

Tuning of PID controlled systems by the rules of Ziegler and Nichols

There are many analytical approaches to design a controller if the plant dynamics are well known, however if there are uncertainties in the process dynamics that need to be approximated this can lead to massive miscalculation and therefore an unstable system. In 1940, Ziegler and Nichols developed tuning rules which were applicable even if the process to be controlled is not well known. These rules were based on extensive numerical calculations and had a big impact on PID-control in its early ages.
Since the step function is something we can evaluate even when the controller is far from the ideal setting, this is a good starting point to set the desired gain constants. The method we will employ is the second developed by Ziegler and Nichols: As a starting point, the integral and derivative action of the controller is tuned to be zero. this can be achieved by setting either the time constants $T_\mathrm{i} = \infty$ and $T_\mathrm{d} = 0$ or the corresponding gain constants $k_\mathrm{i} = k_\mathrm{d} = 0$. Next the proportional gain is increased from zero until the response to the step input shows sustained oscillations. The critical gain K_cr and the oscillation period P_cr at this point are the values the tuning can be based on. According to Ziegler and Nichols the tuning should follow the rules depicted in table 3.1.
Naturally, following these tuning rules will not yield the most optimal response. However, they provide a good starting point for additional adjustments. If one follows the general directions

Table 3.1: Ziegler-Nichols tuning rules based on critical gain K_cr and critical period P_cr [54, Chapter 8-2].

Type of controller	K_p	T_i	T_d
P	$0.5K_\mathrm{cr}$	∞	0
PI	$0.45K_\mathrm{cr}$	$\frac{1}{1.2}P_\mathrm{cr}$	0
PID	$0.6K_\mathrm{cr}$	$0.5P_\mathrm{cr}$	$0.125P_\mathrm{cr}$

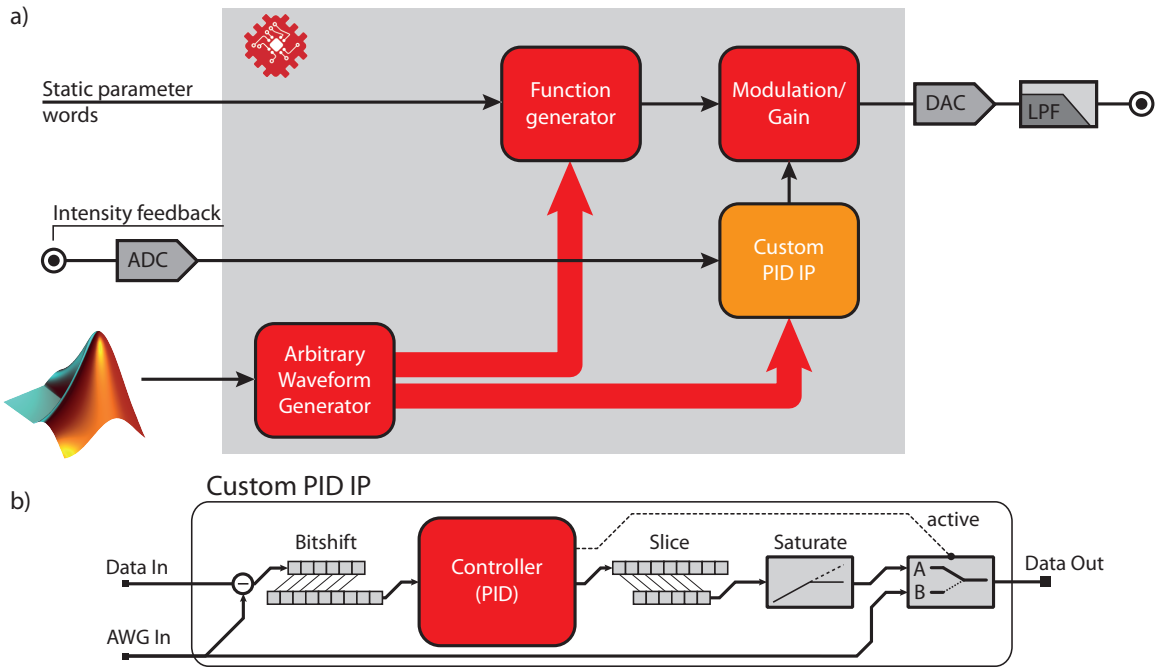

Figure 3.4: a) FPGA functional block diagram with additional PID controller acting on the signal amplitude. The light intensity is monitored by a photo diode and the signal is fed back to the module. The data is used as an error signal for the PID-controller. The setpoint is provided by the AWG, and the PID output replaces the AWG data line as input for the Modulation block. b) Functional block diagram of the modified controller IP. The data coming from the feedback loop is subtracted from the AWG setpoint value, and bitshifted to fit the input of the PID. The output of the PID is sliced and fed to a saturator to reduce its data width to the one used for the amplitude line. Finally, the output data is selected depending on the active bit of the controller – if it is inactive, the setpoint data will be fed through directly. This way it is possible to switch between stabilized/unstabilized operation without having to change the FPGA firmware of the module.

implied by equations 3.13, a well optimized transient response can be achieved.

3.2 Feedback control of phase and amplitude

In chapter 1.3 we established that, in order to deterministically transport atoms within the optical lattice, we need precise control over the phase and amplitude of the light field. In this chapter we introduced the fundamentals of control theory, which we can now apply by extending the system described in chapter 2. The extension of the system is conveniently done by designing the block diagrams for the FPGA structure, which enables the implementation of control blocks.

3.2.1 The FPGA-based PID-controller

The controller we will employ for the stabilization of the phase and amplitude is an intellectual property (IP) provided by Signadyne. The control action can be described with equation 3.1, where in this case the tunable parameters are $k_\mathrm{p}, k_\mathrm{i}$ and k_d. Of course since we are using a

digital controller, the discrete time description of the PID action given in [50] as

$$u_{\mathrm{n}} = k_{\mathrm{p}} e_{\mathrm{n}} + k_{\mathrm{i}} T_{\mathrm{s}} \sum_{n} e_{\mathrm{n}} + k_{\mathrm{d}} \frac{e_{\mathrm{n}} - e_{\mathrm{n\text{-}1}}}{T_{\mathrm{s}}}, \tag{3.16}$$

where T_{s} is the sampling time interval, is the more appropriate choice here. The gain constants can be set via a PC-port memory register, which is also used to activate and reset the module (see Table 3.2). It is important to note here that the gain constant we can set via the register already includes the sampling time, so it holds

$$K_{\mathrm{i}} = k_{\mathrm{i}} T_{\mathrm{s}} = 10^{-8} k_{\mathrm{i}}. \tag{3.17}$$

Originally, the PID controller is designed to be used within the Phase Lock IP we will talk about in section 3.2.3, so to use it as an intensity stabilization tool a few changes have to be made. Figure 3.4 b shows the block diagram of the new IP based on the PID IP. There are several functionalities implemented to make the IP more suitable for our purposes:

Data rescaling: Since the IP is originally meant for the frequency stabilization, its data input and output are not scaled to the 16-bit amplitude words. Therefore the data needs to be shifted to fit the corresponding in/outputs. This can be used to apply a universal gain to the controller by shifting the 16 relevant output bits over the range of the 48-bit data output. This is important, since it directly effects the effective gain range we can apply, and therefore also the coarseness of our gain.

Output saturation: Since the output port is not necessarily protected by the anti-windup functionality due to shifting the output gains away from the most significant bit (MSB), the output resets when it surpasses the maximum value of the 16 bit line going to the Modulation/Gain block, this needs to be prevented. Therefore a saturator is in place which monitors the bits above the output threshold and saturates if necessary.

Setpoint feed-through: The controller features a data valve, that is controlled by the active bit of the IP. This means that if the stabilization is turned off by the memory port interface, the setpoint is fed to the output and the original modulation functionality is still usable.

Figure 3.4 a shows the updated FPGA block diagram. The altered controller IP is placed in between the AWG and the Modulation/Gain block, using the AWG signal as a setpoint y_{sp} and the data read by the analog input port as the actual system value y. The PID acts directly on the Modulation/Gain block and changes the output amplitude depending on y. The Signadyne PID IP has a built in anti-windup functionality, which is partially lost by shifting the output away from the MSB. Windup is a nonlinear effect caused by the integral action during

Table 3.2: Register map of the PID controller IP provided by Signadyne. The values are set by a PC-Port memory register [56].

Value	Size (bit)	Description
Enable	1b	Module Enable/Disable, active high
k_{p}	18b	PID IP proportional gain constant
K_{i}	18b	PID IP integral gain constant
k_{p}	18b	PID IP derivative gain constant
Reset	1b	PID reset, active high

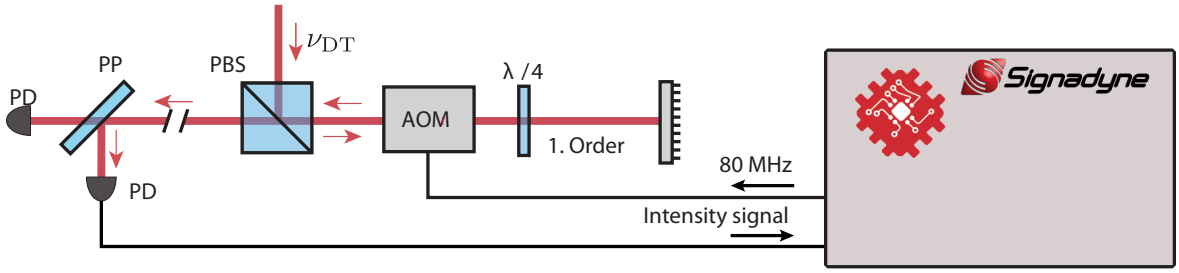

Figure 3.5: Schematic of the setup used to test and characterize the digital intensity stabilization. The light coming from the main TiSa-laser is split by a polarizing beamsplitter cube (PBS), from where it is aligned to an AOM in double pass configuration. The driving signal is coming from the Signadyne module, which uses the feedback signal of a photodiode (PD) to close the feedback loop. An out-of-loop photodiode is used to measure the system response funcion as well as the noise spectrum of the stabilized light beam.

saturation [50]. If for some reason the process saturates without reaching the setpoint value, the error value will remain finite. This means the integrator will accumulate the error and become large, an occurrence known as wind-up. To recover from this, the error has to have a negative sign for an equal amount of time. This can be prevented by saturating the integral accumulator at the maximum output, however this is less effective the further we shift away from the most significant bit of the output.

A notable property is the output delay of the controller. Most operations can be carried out in a parallel manner on the FPGA-chip, so that the computation time is negligible. An addition of a multiple bit value however takes two clock cycles of the FPGA. The overall input to output delay of the custom PID-IP calculation adds up to eight cycles, or 80 ns (60 ns in case of the original PID-block). This is also visible in the brief discussion of the dead time limitation in chapter two (see sec. 3.1.3). Taking the computation time $T_{\mathrm{PID}} = 80\,\mathrm{ns}$ and the input/output delay $T_{\mathrm{IO}} = 453\,\mathrm{ns}$ into account, the theoretical bandwidth of the digital controller amounts to $\omega_{\mathrm{B}} \simeq 1.63\,\mathrm{MHz}$.

3.2.2 Implementation and characterization of an intensity stabilization control loop

In chapter 1.3.1 we already established that the intensity of the light can be influenced by the power of the AOM-driver signal. A schematic of the intensity control setup is illustrated in figure 3.5, depicting the optical setup used to provide the feedback for the digital lock. In the following we will derive a transfer function model for our system which will allow us to identify the system parameters and model the frequency response. As before, we will drop the derivative part in the following calculations, since its marginal effect in a well tuned system.

The process response is mainly dominated by the AOM. The discussion in section 1.3.1 revealed that the dead time is, in fact, the main limiting element of the feedback loop. Hence, we can model the process purely by a dead time element

$$P(s) \equiv \mathcal{F}(\Theta(t-T)) = \exp(-Ts). \tag{3.18}$$

Since the output voltage of the photodiode monitoring the beam intensity is matched to the maximum input voltage of the input port of the FPGA-module, the overall gain of the process

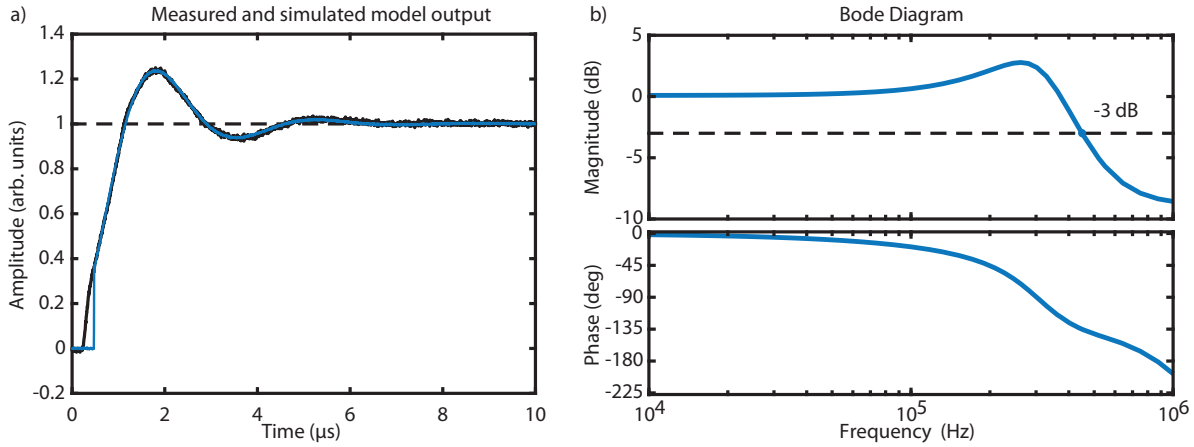

Figure 3.6: a) Step response of the intensity lock (black) and the output of the model identified with Matlab (blue), given a unity step input at $t = 0$ (dashed). b) frequency response of the model system. The top graph shows the magnitude and the bottom graph the phase versus the frequency. The -3 dB crossing of the magnitude (dashed line) indicates the bandwidth of the system.

can be safely assumed to be unity. Combining the transfer function of the controller with the process estimation yields the open loop transfer function

$$L(s) = \frac{k_\mathrm{p} s + k_\mathrm{i}}{s} \exp(-Ts). \tag{3.19}$$

To find an approximation which we can use to identify the system using the transient response characteristics, we have to calculate the closed loop transfer function

$$G(s) = \frac{k_\mathrm{p} s + k_\mathrm{i}}{s + (k_\mathrm{p} s + k_\mathrm{i}) \exp(-Ts)} \exp(-Ts). \tag{3.20}$$

By applying the first order Padè approximation $e^{-Ts} = (1 - \frac{T}{2}s)/(1 + \frac{T}{2}s)$ to the denominator, equation 3.20 can be rewritten as a system of second order

$$G(s) = \frac{a_1 s^2 + a_2 s + a_3}{s^2 + b_1 s + b_2} \exp(-Ts), \tag{3.21}$$

with two zeros and a time delay T, where

$$a_1 = \frac{k_\mathrm{p}}{(1 - k_\mathrm{p})}, \tag{3.22}$$

$$a_2 = \frac{Tk_\mathrm{i} + 2k_\mathrm{p}}{(1 - k_\mathrm{p})T}, \tag{3.23}$$

$$a_3 = b_2 = \frac{2k_\mathrm{i}}{(1 - k_\mathrm{p})T}, \tag{3.24}$$

$$b_1 = \frac{2 + 2k_\mathrm{p} + k_\mathrm{i}T}{(1 - k_\mathrm{p})T}. \tag{3.25}$$

Matlab allows a powerful analysis of such kind of systems, by directly extracting the coefficients 3.23–3.25 from a recorded step response. We measure the step response, which is tuned following the rules established in section 3.1, and insert our model transfer function (3.21) into the toolbox. Figure 3.6 a shows the recorded step response as well as the one which is reconstructed by Matlab, revealing a good agreement between the two. One exception is the initial rise, which cannot be explained by the model, since it is based purely on a dead time approximation. Since we neglected the AOM rise time in our model, it is expected that this behavior is not met. Correspondingly, the dead time extracted by Matlab can only serve as an upper limit.

Through the obtained parameters we can further also study the spectral properties of the control loop, which is shown as a bode plot in figure 3.6 b. This evaluation is based on the frequency response of the system and allows to determine stability margins as well as the overall bandwidth (see section 3.1.2). From the gain bode plot we can deduct a bandwidth of 450 kHz(-3 dB). Further criteria can be obtained by analyzing the frequency response indicators for the stability of the system:

1. The gain margin: The gain margin is the maximum value the gain can be increased before the system becomes unstable. It can be directly read of the bode plot at the point where the phase of the system crosses the -180 degree mark, the so-called phase crossover frequency. In the logarithmic representation it is the difference of the gain curve to unity gain at this point. From figure 3.6 b we can obtain the gain margin to be 8.33 dB.

2. The phase margin: The phase margin is the amount of phase additional phase lag at gain crossover frequency, marked by the frequency for which the gain curve becomes smaller than unity. The phase margin is the difference of the phase at this frequency to -180 degree, the point where the action of the controller is no longer able to dampen, but instead amplifies oscillations. We can read of the phase margin to be 61.8°.

From the stability margins we can conclude that the system is far from being unstable. The phase- as well as the gain-margin are both large enough to leave room for more aggressive tuning parameters, however we do not want to add further oscillatory tendencies to the transient response as the system should return to a steady state as soon as possible after a step. The model system also allows us to check if we have estimated the transfer function correctly by comparing equations 3.23–3.25 to the coefficients of the fitted model (see table 3.3). Especially a_1 and a_3 are of interest for us, as they can be linked to the gain constants of the digital controller. From a_1 we can extract the proportional gain constant $k'_\mathrm{p} = 0.265(1)$. The register value for this particular tuning was $K_\mathrm{i} = 16800$. If we take the 16 bit shift into account we apply to the signal of the controller we arrive at $k_\mathrm{p} = 2^{16} \cdot k'_\mathrm{p} = 17347(707)$, which is remarkably close to the actual value. With this value we can calculate $k'_\mathrm{i} = 661989(23193)$ from equation 3.24. Accounting again for the bitshift as well as the factor originating from the discretized integration (equation 3.17), we can calculate the integral gain to be $k_\mathrm{i} = 2^{16} \cdot 10^{-8} \cdot k'_\mathrm{i} = 433(15)$. The actual register value was 280 which is outside of the error margin, but is still an impressive match considering the strong restriction of the model. As we have seen in section 3.1.2 it is not uncommon for two system parameters to have similar effects and therefore a slight shift in value of two parameters is not surprising.

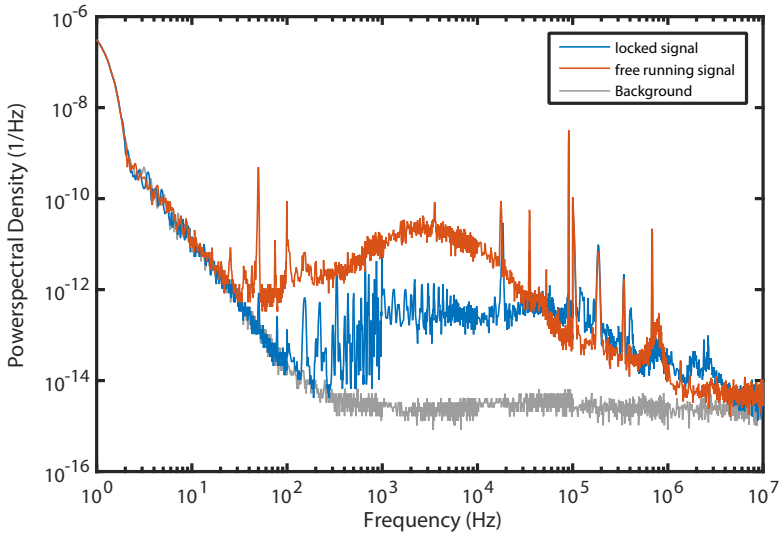

Figure 3.7: Power spectral density relative to the carrier signal at 0 Hz. The spectrum is measured once for the free running system (red) and once stabilized by the digital controller (blue). The background level is measured by blocking the input of the photo diode and measuring the noise level of the output (gray).

Table 3.3: Transfer function model parameters extracted with the Matlab system identifying toolbox for the transient response displayed in 3.6 and the model (3.21).

coefficient	a_1	a_2	$a_3 = b_2$	b_1	T
value	0.36(2)	$1.44(10)\cdot10^6$	$3.9(2)\cdot10^{12}$	$1.5(8)\cdot10^6$	$4.76 \cdot 10^{-7}$

Intensity noise suppression

Now that we have thoroughly analyzed the system behavior it is time to take a look at the noise suppression. For that purpose we measured the one-sided spectral density of fractional amplitude fluctuations of the laser intensity, which is illustrated in figure 3.7. This measurement is carried out via an out of loop photodiode (see fig. 3.5) connected to a spectrum analyzer[1] – once for a free running laser beam and once stabilized by the controller described above. The V^2/Hz values have been converted to fluctuations relative to the lattice intensity $S_a(f)$, by normalizing the data to the squared DC voltage value of the photo diode. The one-sided spectral density is defined as $1/2 \times S_a(f)$ [39].

The spectrum shows several spurious peaks, which are however related to the measurement environment: For example, the prominent peak on the lower end of the spectrum originates from the power line frequency at 50 Hz, and the most significant peak at 90 kHz is caused by the etalon lock of the titanium-sapphire (TiSa) laser [57]. This modulation is several orders of magnitude above the common noise floor, and causes the major part of fluctuations of the lattice – for both intensity and phase. For frequencies $f \leq 50$ kHz the noise suppression achieves a reduction of noise of up to two orders of magnitude. For higher frequencies the noise floor

[1] Hewlett Packard Network Analyzer 3589A

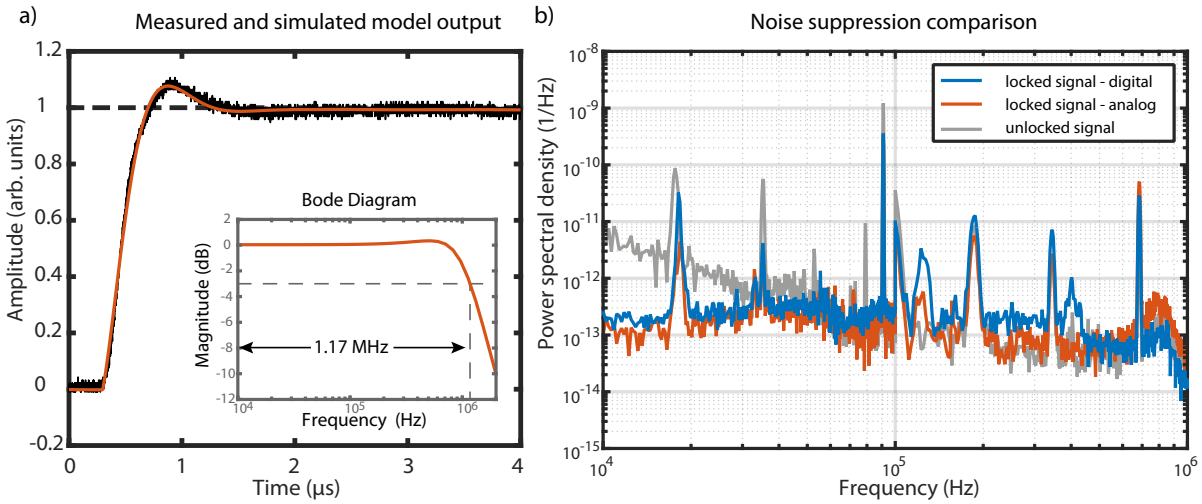

Figure 3.8: Characterization of the analog intensity controller by Vescent. a) Step function and simulated model of the system, with corresponding bode magnitude plot. b) Power spectral density comparison of the noise of the digitally and analog controlled intensity.

seems to be below the sensitivity threshold of the controller. This is in contrast to the preceding analysis, which extracted a much higher bandwidth of 450 kHz. For a better comparison, we repeat the analysis with a well known analog lock circuit[2], which is discussed in the following section.

Comparison to an analog controller

To benchmark the performance of the digital control loop, the test setup is stabilized and characterized using the control setup currently employed in the one-dimensional quantum walk laboratory. The exchange is simple, as the analog lock can be applied by employing a mixer to actively attenuate the signal power[3], provided by the Signadyne vector generator. The analysis follows the same procedure as for the digital lock, described in the preceding section. From the step response and the corresponding bode plot, shown in figure 3.8 a, a bandwidth of 1.2 MHz can be inferred, which is expected, since the analog controller has a bandwidth of 12 MHz, whereas the digital one itself is limited to 1.63 MHz (see sec. 3.2.1). However, the noise suppression shown in figure 3.8 b shows no significant difference between the analog and the digital stabilization.

3.2.3 Implementation and characterization of the optical phase lock loop

In this section I will explain the implementation of the phase locked loop into the structure of the digital system. To be able to talk about the step response and analyze the system behavior in a similar way as for the intensity stabilization, it is necessary to give a detailed overview over the final setup, the polarization synthesizer. In section 1.3 we already established the physical concepts to achieve state dependent transport by synthesizing the polarization. In this section I will give further details regarding optical setup and the opto-electronic phase lock loop.

[2] Vescent Lockbox, as used i.e. in Robens [14, Chapter 2.1.2]
[3] We employ a Mini-Circuits ZX05-1-S+ Mixer, as described in [58].

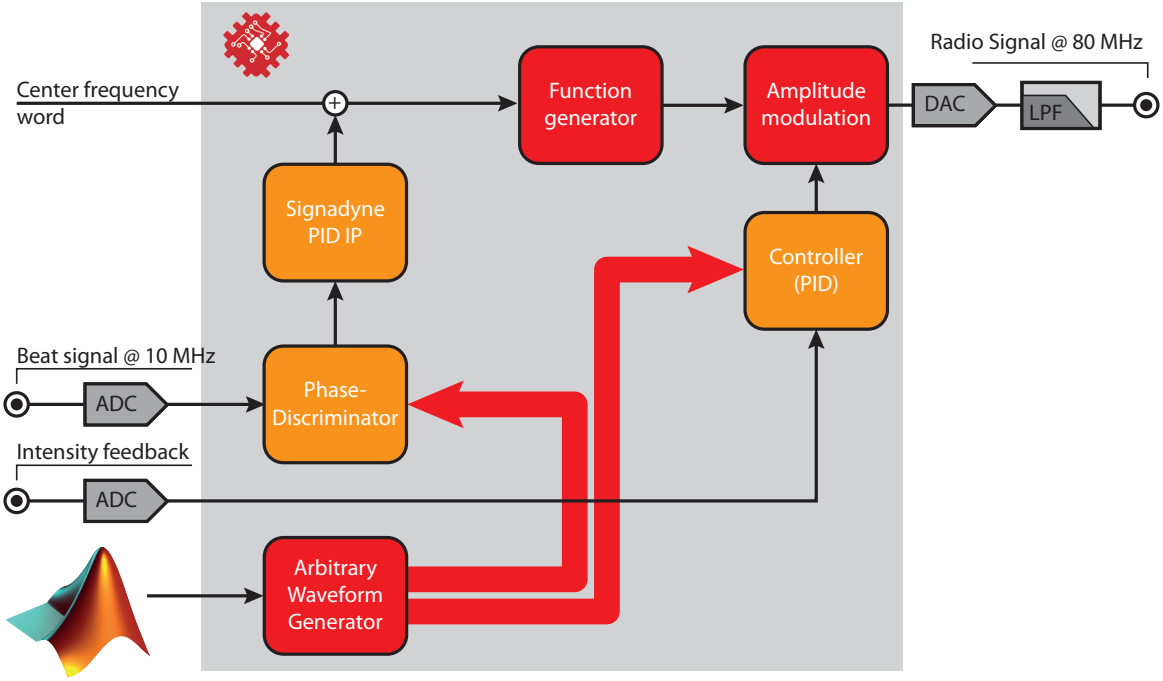

Figure 3.9: Functional block diagram of the FPGA firmware with integrated phase/frequency lock capability. The center frequency word routed to the Function Generator is updated with the corrections from the phase lock loop. The correction is calculated by a PID module, which itself receives its error signal from a digital Phase-Detector block developed by Signadyne. The phase detector is designed to measure phase and frequency difference of input data against an internal reference and combine them as a single error signal around zero.

Implementation of a digital phase lock

The implementation of the digital phase lock loop is made possible by the Phase Lock Loop FPGA-module (PLL-IP) which has been developed by Signadyne specifically for the purposes of our group. Therefore, the detailed code of the FPGA-module is not available. The specifications of the module can be found in the data sheet [59]. The module can be viewed as an extension of the PID-controller module introduced in section 3.2.1, as it combines it with a digital phase detector into a standalone unit. For a more intuitive picture, the functional block diagram – shown in figure 3.9 – illustrates the phase detector and the controller IP as separate blocks, however, in reality they are fused together. The register values are extended by the phase- and frequency-specific parameters, which are listed in table 3.4.

The working principle of the phase detector is divided in two parts: First, the reference signal data is accumulated and stored to be compared against the data provided by the internal reference frequency. To achieve the best results, the accumulator should be chosen such that the accumulation period $n\,t_s$ is a multiple to the inverse of the signal frequency; This ensures a dataset with complete periods only.

If the frequency of the signal is far off, the module applies rough frequency corrections to get into a range where the phase difference of the two signal does not deviate by more than 2π in one measurement cycle. Once the phase does not deviate more than 2π during this period, the unit switches to a more precise measurement method, involving a fast Fourier transform. One

measurement cycle in this case is defined by the data conversion stages taking in total 32 FPGA clock cycles, which for a clock frequency of 100 MHz corresponds to a duration of 320 ns. The digital phase measurement on the FPGA chip is convenient, but it can not compete with the quickness of an analog signal. The fast Fourier transform carried out to discriminate the phase is an iterative process, which makes the parallelization of the calculation unfeasible. Another factor is the accumulation of the analyzed data. We chose typically an accumulator size of 30, which increases the computation time by 30 cycles, or 300 ns. This has to be considered when evaluating the performance of the system, since the phase measurement adds additional dead time to the closed loop.
The corrections of the two measurements are available on two output ports for monitoring, and are further processed and merged into a single error signal around zero to be sent to the controller. The controller output is a 48 bit frequency value applied to the Function generator in addition to the frequency word.

An important property of the PLL-IP is a phase and a frequency input, each in addition to the register value. Since the reference frequency is where we can apply the setpoint value, it is important we can provide it via the AWG data with the usual timing precision (see sec. 2.1.4). The data received by these inputs are added to the values set by the register memory.
Due to the sampling rate limitation of 100 MHz, the frequency stabilization has a limit of 50 MHz, defined by the first Nyquist zone. To increase the number of samples per period, and therefor the precision, we decided to choose a lock-frequency of 10 MHz. In principle this can be changed to any value, as we will further discuss in section 3.2.3. To quantify the influence of the phase lock loop, the phase noise with active phase lock is compared to the measurements of the basic system discussed in section 2.3.

Phase noise influence of the digital phase lock loop

In the following section I will discuss the influence of the active phase lock loop on the phase noise of the output signal of the Signadyne module. As a first compare the pure electronic signals by To characterize the electronic phase noise of the locked signal it is measured as already discussed in section 2.3. In this case, one of the signals is splitted and fed back to the input port connected to the phase lock unit on the FPGA, displayed in figure 3.9. The setup for the measurement is sketched in figure 3.10 a, and the corresponding measured data is shown in b. The data is once measured for the free running module at 10 MHz (yellow) and once for the locked channel (green). In both cases the reference for the mixer is a free running channel at

Table 3.4: Register map of the PID controller IP provided by Signadyne. The values are set by a PC-Port memory register [56].

Value	Size (bit)	Description
Frequency	32b	Internal reference signal frequency
Phase	32b	Internal reference signal frequency
Acc_size	10b	Number of data accumulation samples
Phase_range	16b	Phase range in which the signal is considered locked
Frequency_range	16b	Frequency range in which the signal is considered locked
Phase_reset	1b	Internal reference signal phase reset, active high
PID parameters	18b	PID parameters as described in section 3.2.1

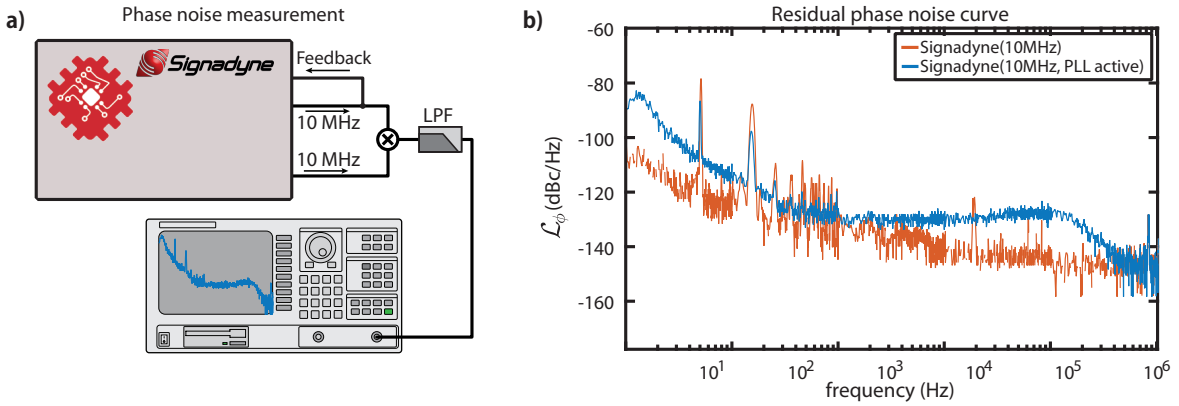

Figure 3.10: Phase noise measurement setup and comparison of different working modes of the Signadyne FPGA-module. a) Schematic of the phase noise measurement technique. Two signal channels of the same center frequency are mixed by a phase discriminator and the difference frequency is isolated by a low pass filter. This signal is fed to a spectrum analyzer to extract the spectral density of the phase signal. In this case, one of the channels is phase locked by the digital PLL-IP, which corresponds to the measurement plotted in blue in part b) of the figure. b) Phase spectral density with respect to the carrier signal. The two datasets show the difference in phase noise of the purely electronic signal, when the phase lock loop(PLL) is activated.

10 MHz. In both cases the background measurement has been subtracted, which causes residual peaks towards the end of the spectrum, where the difference between measured noise and the background is close to zero.

The data is compared against the measurement discussed in section 2.3 (blue). The spectrum shows several spurious peaks at multiples of the power-line frequency 50 Hz. These can be removed by carefully adjusting the electronic lines such that they pick up less noise from power lines in close proximity of the setup. The effect of the electronic phase lock is more severe: The amount of phase noise is increased by several dB over the entire spectrum reaching almost two orders of magnitude in the range of 100 kHz. Possible sources for the increased phase noise are the additional analog to digital – and vice versa – conversions, which each deteriorates the signal further. An additional factor is the internal reference frequency – which has an unknown phase noise since it cannot be directly measured – but is assumed to be on the same order as the free running signals. Despite the overall increase phase noise, phase lock is very well suited for our needs, since the overall in lock phase noise corresponds well to the respective spectrum of the one-dimensional experiment. Nevertheless, future applications could improve the phase noise by including a sophisticated analog phase discriminator into the module, which could increase the precision of the phase lock loop tremendously. Another approach could be the DDS of the reference channel. Replacing it with a more precise unit might boost the performance already, without having to change the hardware at all. These approaches of course require extended collaborations with Signadyne, and should be well researched before committing to such measures. In the following, we will introduce the optical phase lock loop and how it is used to create a synthesized polarization following the outline given insection 1.3.

The optical phase lock loop setup

In the following, we will introduce the opto-electronic setup used to apply the phase lock to a the light field of a laser beam, and then thoroughly characterize the control bandwidth of the

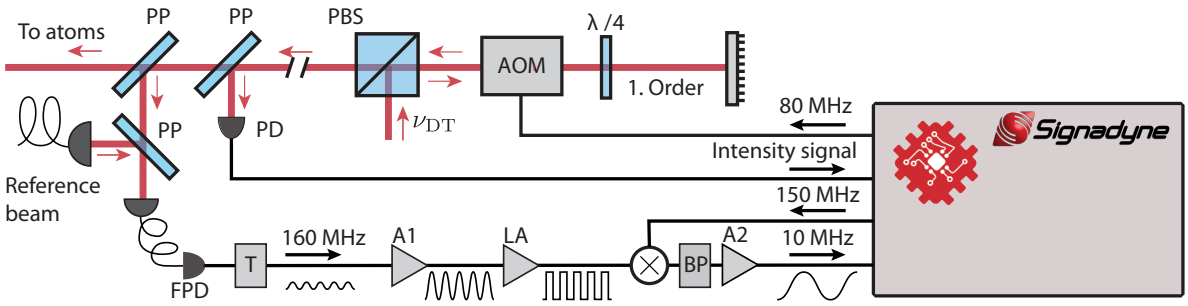

Figure 3.11: Optoelectronic setup for the simultaneous phase and amplitude stabilization of a laser beam. $\nu_{DT}$is the frequency of the dipole trap beam(red), with arrows indicating the propagation direction. Abbreviations used are: Polarizing Beam Splitter(PBS), Acousto-optic Modulator(AOM), Quarter-Wave-Plate($\lambda/4$), Pickup Plate(PP), Photodiode(PD), Fast Photodiode(FPD), Bias-Tee(T), Amplifier(A), Limiting Amplifier(LA), Bandpass Filter(BP). The figure as well as the setup design are adapted from the initial design published in Robens [14, chapter 3.2.1]

optical phase lock loop (OPLL). The optical as well as the electronic setup are based on the findings already published in [27], and have only been adapted to the different circumstances of this experimental setup. In Section 1.3 we already established the concept of polarization synthesis by controlling the phase and amplitude of two light beams with perpendicular circular polarization.

The digital control system for amplitude and phase stabilization was introduced in sections 3.2.1- 3.2.3, so that we can now include this concept in the optical setup to experimentally realize a light beam with well defined phase and amplitude. The stabilization setup for one of the two constituting light beams is displayed in figure 3.11. The light beam coming from the dipole trap laser is modulated by an AOM in double-pass[4] configuration, which shifts the frequency of the light twice by the driving radio-frequency of 80 MHz. A quarter-wave-plate rotates the polarization of the light, so it passes the polarizing beam splitter cube (PBS) on the return path. The intensity feedback signal is measured by a fast photo diode using a portion of the light reflected from a pickup plate. In order to extract a lock signal for the OPLL, the light is overlapped with a reference beam which was not modulated by the AOM, such that the interference creates a beat signal at the difference frequency of 160 MHz. The two beams are coupled into a fiber which is directly connected to a fast photo diode[5]. A bias tee[6] provides the bias voltage of the photodiode in order to isolate the oscillatory beat signal. A low noise amplifier[7] is employed to increase the signal power. This is supported by a limiting amplifier[8] to ensure a constant output power independent from the amplitude of the initial signal. This prevents possible amplitude to phase conversions by limiting the signal to either positive or negative maximum output. The signal prepared in this manner is down-converted by mixing it[9]

[4] The double pass introduces a factor of 2 in the otherwise unitary phase translation of the AOM. This is in case of the lock signal compensated by the controller-gain constants, for direct modulation this can be corrected by applying a modulation gain of $[-\pi/2 : \pi/2]$ instead of $[-\pi : \pi]$
[5] Hamamatsu Ultrafast MSM Photodetector G4176 series
[6] Mini-Circuits Bias-Tee ZX85-12G+
[7] Mini-Circuits noise amplifier ZFL-500HLN+
[8] Analog Devices Limiting-logarithmic amplifier AD8306
[9] Mini-Circuits ZX05-1-S+ Mixer

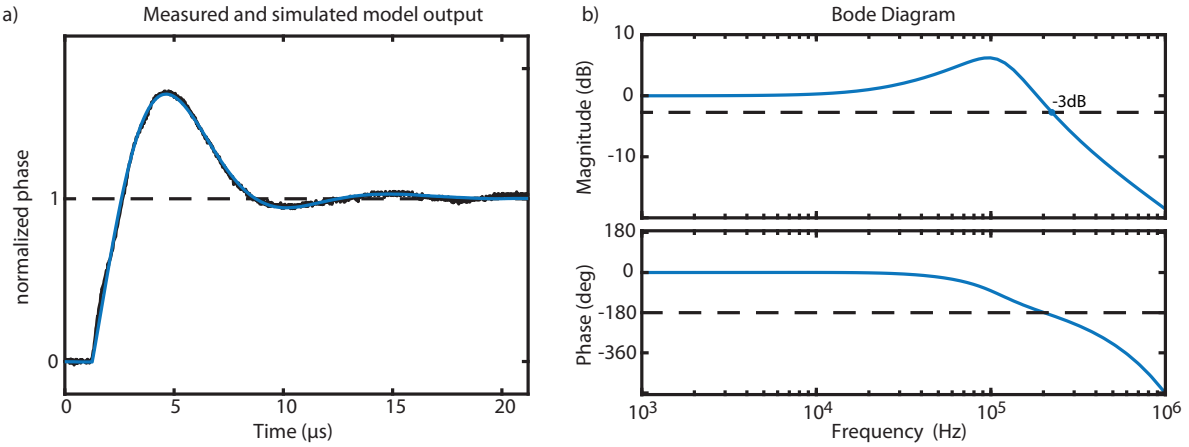

Figure 3.12: Characterization of the OPLL measured step response by the fit of an analytical model. a) Transient response of the OPLL (black) and simulation of the model system (blue). The setpoint is changed by 10° at $t = 0$. b) Frequency response of the system extracted from the fitted model. The dashed lines mark the -3 dB threshold in case of the magnitude plot, and the -180° margin for the phase plot.

with a stable 150 MHz reference, and the difference of 10 MHz is isolated by a band pass filter[10]. The band pass filter also reverts the rectangular shape formed by the limiting amplifier, since it filters out the higher harmonics of the signal. The 10 MHz signal is again amplified to have an amplitude of 200 mV, which can be read by the Signadyne module DACs, and analyzed by the digital phase lock introduced in section 3.2.3. The correction is then applied to the driving signal of the AOM which closes the feedback loop.
The lock frequency of 10 MHz is chosen virtually arbitrary, by setting the frequency of the mixer reference and the internal lock frequency accordingly. By choosing e.g. a lower frequency, the precision of the phase detection could be increased, due to the increase of samples per period. However, this is not tested in this case but might be worth investigating in the future.

Characterization of the optical phase lock loop

To measure the step response of the phase lock loop, we make use of the basic principles introduced in section 1.3, by overlapping two phase and amplitude controlled beams (see also sec. 4.1). From equation 1.11 it follows that a phase ramp applied to one of the phases $\phi_\uparrow$ or $\phi_\downarrow$ results in a rotation of the linear polarization vector of the combined light fields. The beam intensity is measured through a linear polarizer under 45° configuration, such that it acts as a phase to intensity converter. This way we can deduct the step response of the controlled system, shown in figure 3.12 a.

To apply a similar theoretical model as for the intensity control-system in section 3.2.2 we need to take two differences of the phase control system into account, the first of which is the dead time T, which is increased by the phase measurement duration of the phase detector module (see sec. 3.2.3). Including this with the dead time of the AOM process, and counting

[10] Mini-Circuits SBP-10.7+, 9.5-11.5 MHz Bandpass Filter

the additional calculation of the PID, the estimated dead time comes out to

$$T = T_{\mathrm{AOM}} + T_{\mathrm{Accumulator}} + T_{\mathrm{FFT}} + T_{\mathrm{PID}} \approx 1.2\,\mu\mathrm{s}. \tag{3.26}$$

A further difference to the model system we applied in 3.2.2 is the control action itself. Since we apply the corrections of the controller to the frequency word input of the function generator, we are dealing with a so-called integral process. This configuration is fundamentally not ideal, since the possibility exists to act directly on the phase. However, this would call for a re-development of the phase lock module, which can in principle be done but is not covered in this thesis.

The current configuration adds a further integration to the open loop transfer function, such that it changes from 3.19 to

$$L(s) = \frac{k_{\mathrm{p}} s + k_{\mathrm{i}}}{s^2} \exp(-Ts). \tag{3.27}$$

This means that the closed loop transfer function and our characteristic polynomial will be of third order. Calculating the closed loop transfer function and applying again the first order Padé approximation to the exponential term of the denominator yields

$$G(s) = \frac{k_{\mathrm{p}} s^2 + (\frac{2k_{\mathrm{p}}}{T} + k_{\mathrm{i}})s + \frac{2k_{\mathrm{i}}}{T}}{s^3 + (\frac{2}{T} - k_{\mathrm{p}})s^2 + (\frac{2k_{\mathrm{p}}}{T} - k_{\mathrm{i}})s + \frac{2k_{\mathrm{i}}}{T}} \exp(-Ts). \tag{3.28}$$

Figure 3.12 a shows the transient response of the system for an input step of 10 degree at $t = 0$, and the simulated response of the model fitted by the Matlab system identification toolbox. In this case the model agrees remarkably well to the experimental data. This increased dead time leads to a reduced stabilization bandwidth of 230 kHz, as indicated by the bode plot in figure 3.12 b. The stability margins ins this case can be extracted to be a gain margin of 1.32 dB and a phase margin of 11.12°. These values still indicate a stable system, but the margins are small compared to the ones of the intensity controller. This is also indicated by the overshoot of 65 %, which has to be accepted in order to reach a reasonable response speed. Overall, the systems response is not optimal, and could be retuned to be less aggressive, sacrificing control speed for larger stability margins.

Since the phase detector module has an unknown transfer function, the parameters cannot be matched in this case as we did in 3.2.2. However, it is save to assume that the transfer function is linear and not frequency dependent, which means it only applies an unknown scaling factor to the system that is compensated by the tuning parameters.

To measure the differential phase noise between the two polarization components of the light we follow the procedure laid out in [14, 3.2.2]. The light is monitored through a linear polarizer at 45° angle, such that the intensity is directly proportional to the polarization angle $\Delta\phi = \phi_\uparrow - \phi_\downarrow$ (see section 1.3). The conversion factor between phase and amplitude can be extracted by applying a constant phase ramp to one of the phases $\phi_\uparrow, \phi_\downarrow$. This way, the linear polarization vector can be rotated, and the resulting sinusoidal signal shape can be used to extract the conversion factor

$$K_\phi = A\frac{d\sin(0)}{dt} = A\frac{V}{rad} \tag{3.29}$$

at the measurement point. The differential phase spectral density $\mathcal{L}_\phi(f)$ can then be calculated by proceeding as described in section 2.3. In this case, the data is reduced by the background given by the intensity noise measured at 0 degree angle between the linear polarization and the analyzer axis, which yields no phase dependence in first order. Figure 3.13. a and b show the

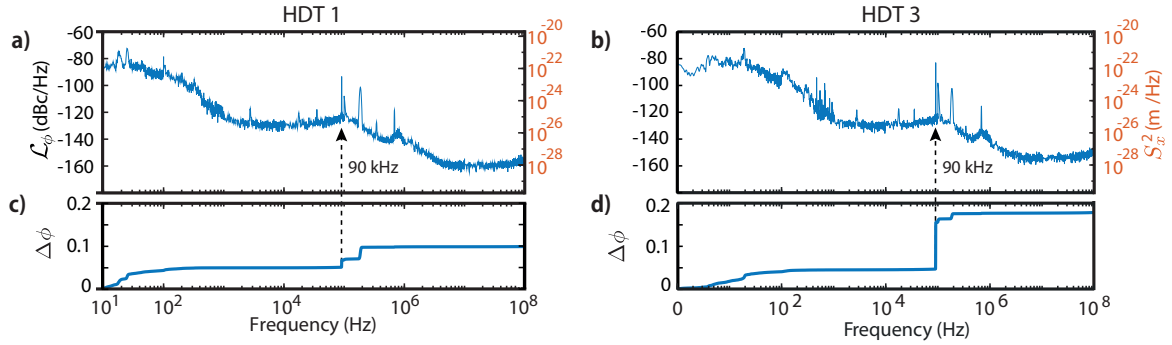

Figure 3.13: Phase spectral density of the two polarization synthesized lattice beams HDT 1 and HDT 3 (HDT = Horizontal Dipole Trap). The data is plotted in a) and b) in decibel relative to the carrier power. The conversion to deviations in m^2 per Hz is given in red on the right axis. The dashed line marks the 90 kHz frequency peak caused by the etalon lock of the main laser. c) and d) show the cumulative phase jitter for the respective spectrum.

phase noise of the two polarization synthesized horizontal dipole trap arms HDT 1 and 3 (see sec. 4.2, while the cumulative phase jitter $\Delta\phi$ is presented in c and d. The phase fluctuation can be converted into relative lattice position by using equation 1.6 from chapter 1.3:

$$\Delta x = \frac{\lambda}{\sqrt{2}} \frac{\Delta\phi}{2\pi}. \tag{3.30}$$

In the final setup we employ two polarization synthesized arms HDT 1 and HDT 3 (Horizontal Dipole Trap, see sec. 4.2). The total respective phase jitter sums up to $\Delta\phi_1 = 0.17°$ and $\Delta\phi_2 = 0.099°$), which amounts to $\Delta x_1 = 2.89\,\text{Å}$ and $\Delta x_2 = 1.68\,\text{Å}$. The two values show a noteworthy discrepancy, which nonetheless can be explained by the cumulative sum taken of the phase noise. The majority of the phase jitter originates from the peak at 90 kHz, marked by the dashed lines in figure 3.13. This peak is caused by the etalon lock of the TiSa laser and is therefore also present on the reference beam [57]; This way it does not show on the beat signal to the full extend, such that it surpasses the optical phase lock. The discrepancy between the phase jitter values is caused solely by the difference in height of the peak at the times the data was taken. Disregarding the steep increase at 90 kHz and the second harmonics at 180 kHz reduces the overall phase jitter to $\Delta\phi = 0.05°$ in both cases. This translates to a position displacement of $\Delta x = 0.83\,\text{Å}$.

3.3 Increasing response speed with feedforward control

When the dead time of the controller is significant, the performance of traditional control schemes is limited drastically, as we have seen in section 3.1.2. In engineering and control theory in general, this issue is well known and there are several well researched modifications to the traditional controller design to prevent limitations caused by pure input/output lag [60, 61, 62]. The main premise is the usually well known system response, which can be simulated and compensated in real time. This way, the delay caused by the dead time can be disregarded when tuning the controller. In the following section I will introduce the general design of such a controller and comment on the implementations into the FPGA system.

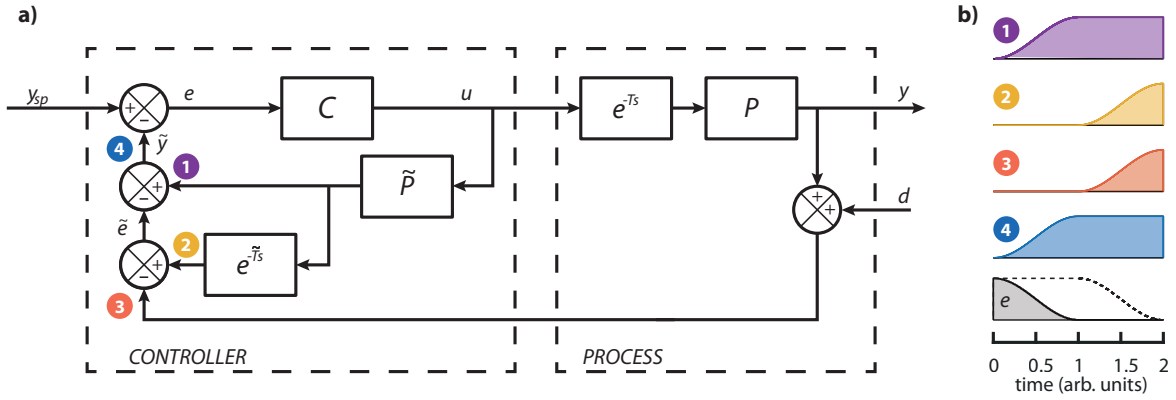

Figure 3.14: Illustration of Internal Model Control. a) Block diagram of a feedback loop with additional feedforward model control. The basis of the control loop is designed as the one discussed in 3.1.2. The additional feedforward loop is implemented by employing a process model $\tilde{P}$ (1), which is designed to match the process P. The model output is fed back to the controller, closing the internal feedback loop. To take the actual system response y into account, the output of the process model is split and delayed by T, which completes the process model (2). Only the difference $\tilde{e}$ between the actual process reaction (3) and the model is noticed as a disturbance in the error signal e. This way, also deviations of the model from the process are accounted for, after one dead time period T. b) Exemplary time traces for a unit step input at $t = 0$ at different points in the diagram, and the resulting error signal e. The dashed line indicates the error signals without, the solid line with IMC. If the model $\tilde{P}$ is perfect, the contributions from (2) and (3) cancel each other out, such that $\tilde{e} = 0$.

3.3.1 The internal model controller design

The most common dead time compensation solution is the Smith predictor. It can be understood as an extension of the classical controller design discussed in section 3.1, and arose to increase the control speed of systems with pure dead time components $P' = Pe^{-Ts}$. The concept aims to design a controller which is tuned to achieve a satisfactory closed loop response to the system CP, and therefore is not limited by the dead time component of the process. A schematic illustration of the controller design is shown in figure 3.14 a – with exemplary illustrated time traces shown in b. It relies on a model of the process P, denoted as $\tilde{P}$, which is simulated within the controller. If C is designed with regard to $\tilde{P}$, the closed loop response of the internal system (1) will be significantly faster due to the lack of dead time limitation.

The actual process can react just as fast despite of the dead time, if the controller output is applied as an open loop input of the system CPe^{-Ts}. Nevertheless, the outer feedback loop still needs to be closed in order to be able to react to disturbances d. This loop is however carrying outdated information, as the internal model has already provided the feedback for the controller. Therefore the process reaction is canceled out by a third feedback loop, carrying the delayed model response $C\tilde{P}e^{-\tilde{T}s}$, where $\tilde{T}$ is tuned to match T. This way, only discrepancies between model and process will be fed back as disturbances.

Following the block design the feedback of the controller amounts to

$$\tilde{y} = y_{\mathrm{sp}} \left[CPe^{-Ts} + C\tilde{P} - C\tilde{P}e^{-\tilde{T}s} \right]. \tag{3.31}$$

If we assume a perfect model of the process is employed, we can substitute $P = \tilde{P}$ and $T = \tilde{T}$,

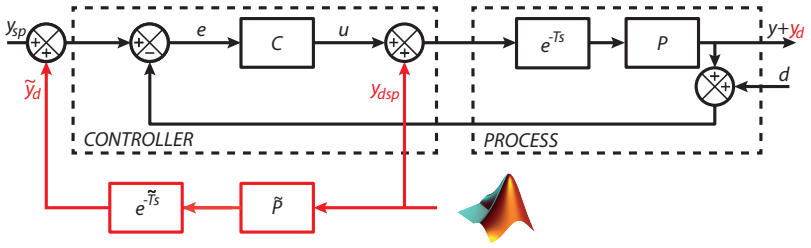

Figure 3.15: Functional block diagram of the IMC control structure implementation to the phase lock loop. The basic phase lock implementation has been extended by an additional AWG data line routed directly to the Function generators phase modulation input. The two data streams supplying the setpoint data to the intensity and phase lock module are still in use, so that the additional AWG has to be removed from another output channel.

such that the response of the system reduces to

$$\tilde{y} = C\tilde{P}y_{\mathrm{sp}}, \tag{3.32}$$

which is the equivalent to the feedback of the system for a time delay $T = 0$.
In reality, a perfect match of a model is of course not easy to achieve. Discrepancies between process and the model will be noticed by the controller after one dead time period and counteracted together with disturbances d. This behavior was already observed in Seidler [63], where the mismatch of the model was noticeable through kinks in the transient response function, showing in regular intervals of the dead time T.
Furthermore, it is important to note at this point, that the disturbance rejection of the controller is not improved in the same way as the ability to follow a setpoint. The sensitivity function of the controller still is affected by the dead time.

The initial approach to apply the feedforward control to the phase lock loop was to implement a similar model as discussed in this section on the FPGA unit, computing the process model to given inputs in real time; However, since we are dealing with a modulo system, we have to take another difficulty into account. While shifting the atoms over multiple lattice sites, the phase value undergoes frequent jumps of $\pi \rightarrow -\pi$. This needs to be accounted for in the process model, which has a fixed input/output range, in contrast to the digital phase discriminator, where the comparison to the reference yields the intrinsic relation $-\pi = \pi$. While the initial approach proved to be not feasible without extensive development of a sophisticated process model FPGA-IP, it is still possible to implement a variation of the Smith predictor by taking advantage of the properties of our system.

3.3.2 Implementing feedforward phase control

Figure 3.15 b shows the updated controller schematic inspired by the smith predictor discussed in the previous section. We can take advantage of the operation mode of our system to change up the internal model control structure.
The goal of feedforward control is to ensure user inputs are not delayed by the control loop transient response. Setpoint changes should apply to the system as fast as possible, without

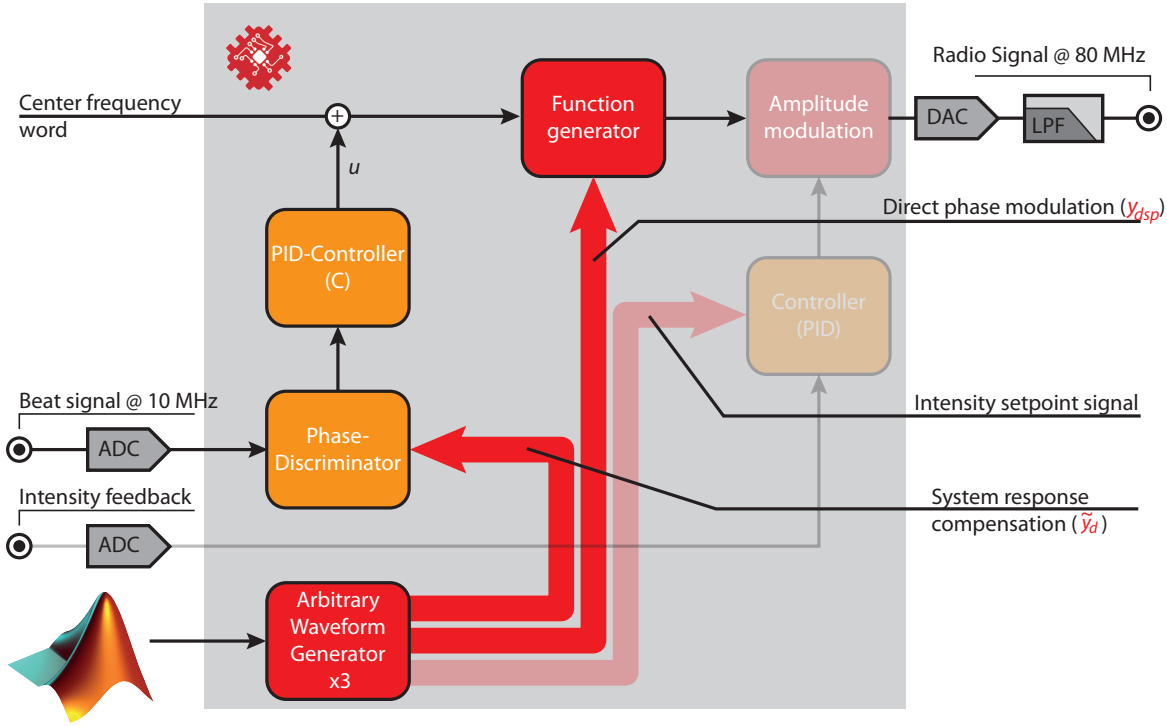

Figure 3.16: Functional block diagram of the IMC control structure implementation to the phase lock loop. The basic phase lock implementation has been extended by an additional AWG data line routed directly to the Function generators phase modulation input. The two data streams supplying the setpoint data to the intensity and phase lock module are still in use, so that the additional AWG has to be removed from another output channel.

disturbing the steady state of the control loop.

The advantage we have over most of the systems addressed by control theory is the pre-planned experimental sequence (see sec. 2.1.4). Controllers like the smith predictor are usually used to compensate dead time for processes that have arbitrary inputs, e.g. the setpoint should be able to change at any point in time without any preparation. This is not the case in our system. As we discussed briefly in section 2.1.4, the experiment is controlled by designing a sequence with nanosecond precision, which is then loaded to the hardware and executed to carry out a measurement or calibration. This fact sets the system apart from the general feedforward problem: it is known exactly when the setpoint changes will occur, and it is known a (relatively) long time in advance. Due to this fact the process model calculation and compensation can be applied already when compiling the sequence. This is indicated in red in figure 3.15 b. Changes that should occur immediately can be separately injected to the control action u as a direct setpoint y_{dsp}. These changes are directly applied to the system and produce the system output

$$y_{\mathrm{d}} = y_{\mathrm{dsp}} P e^{-Ts}. \tag{3.33}$$

To prevent the controller from acting on such direct system changes, the model control loop produces a similar response, by applying a model of the system

$$\tilde{y}_{\mathrm{d}} = y_{\mathrm{dsp}} \tilde{P} e^{-\tilde{T}s} \tag{3.34}$$

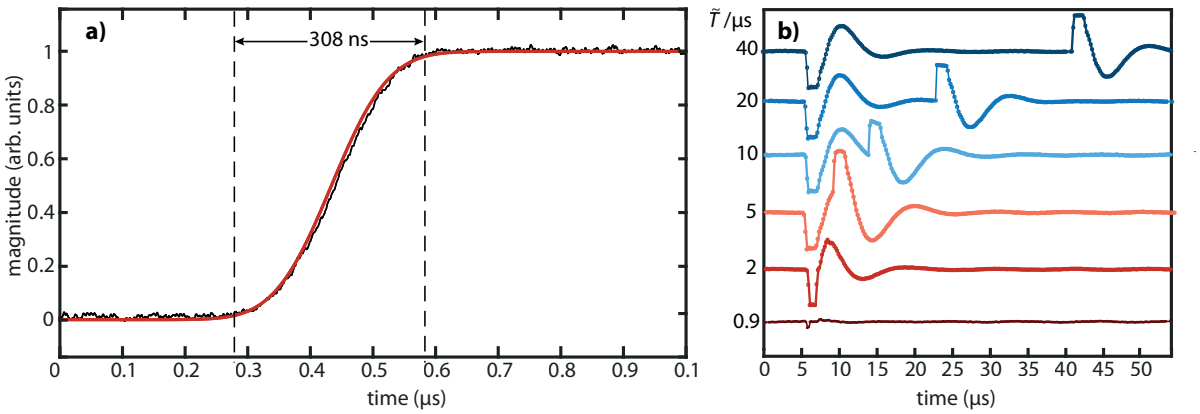

Figure 3.17: Measured data of applied internal model control. a) Phase transient response to a 20° step applied directly to the function generator as described in section 3.3.2. The data (black) is fitted with a normalized error function (red). b) Digital error signal when applying a transport step to the function generator and the compensation to the setpoint of the controller after a delay time $\tilde{T}$.

which is merged with the setpoint signal stream y_{sp} and subsequently sent to the controller. This yields an error signal e which is not affected by the direct setpoint injection

$$e = y_{\mathrm{sp}} + y_{\mathrm{dsp}} \left(\tilde{P} e^{-\tilde{T}s} - P e^{-Ts} \right) \approx y_{\mathrm{sp}}, \tag{3.35}$$

where we again assumed a perfect model $\tilde{P} e^{-\tilde{T}s} - P e^{-Ts}$.
To implement this into the digital phase lock loop, we need to make some changes to the phase control system. Figure 3.16 shows the FPGA PLL structure with already implemented feedforward control. The key difference is the way we apply time critical phase ramps: we use an additional AWG signal to directly modulate the phase at the frequency generator, and thereby bypass the phase lock loop; This means that the phase change is applied directly, only processed by the AOM response. The internal model compensation is applied to the corresponding part of the experimental sequence. Since the two data streams are executed simultaneously by the AWG, so that the dead time approximation can be precisely tuned by monitoring the remaining error signal during a step. The correction can be applied entirely in advance, by convolving the phase time trace y_{dsp} applied to the function generator with the error function fitted to the AOM response. If the simulated model of the system response $\tilde{y}_{\mathrm{p}}$ is included in the phase input sequence y_{sp} compiled for the reference of the phase detector module on the FPGA, the system response y_{sp} is compensated. Since the phase translation of the AOM is perfectly linear, the only parameter which needs to be taken into account to meet the system response is the rise time of the AOM.

3.3.3 Transport ramp performance improvement

The improved transport ramp is measured by injecting a 20° phase step directly to the function generator following the design presented in the previous sections. To measure the phase response, it is mapped onto an amplitude signal as described in the previous chapters (see sec. 4.1). Figure 3.17 a shows the optimized step response of the system. The time trace of the system is defined by the AOM response function (see sec. 1.3.1). This allows us to describe the system response

as a pure error function in the time domain

$$\frac{1}{2}\left(1+\operatorname{erf}\left(\frac{t-\mu}{\sigma\sqrt{2}}\right)\right), \tag{3.36}$$

which is the cumulative distribution function of the Gaussian beam shape. The fitted function plotted in red yields the parameters $\mu = 437.4(2)\,\mathrm{ns}$ and $\sigma = 68.4(4)\,\mathrm{ns}$. The rise time of $t_r = 308\,\mathrm{ns}$ is in good agreement with the AOM response we discussed in section 1.3.1. This analytical function can be well converted into frequency space, by taking the derivative of the fitted function, which results in the original Gaussian beam shape, translated to the time domain by the acoustic travel velocity in the AOM. The Laplace transform of this function yields a Gaussian in frequency space with a width of $\sigma' = 1/\sigma = 14.706(85)\,\mathrm{MHz}$ in frequency space [64].

Figure b shows the internal error signal of the phase detector on the FPGA unit. This data can be monitored by routing the phase output of the phase detector to one of the DAQs. The data is acquired using the analog trigger functionality which we briefly discussed in section 2.1.5. By supplying the trigger from an additional data line on the FPGA the error stream can be monitored in correlation with the step input. The figure shows the response signal for a step input y_{dsp} supplied to the function generator, and the compensation $\tilde{y}$ provided after a time delay T_{D}. For this case – as the convolution algorithm is not implemented yet – the compensation consists only of the delayed input step. The data shows nevertheless the effect of the controller design. This is a result of the working principle of the digital phase detector (see sec. 3.2.3). The measurement duration of the phase detection is 320 ns, such that the entire response does not exceed one measurement cycle. Each data point in figure 3.17 b corresponds to such a cycle. As the dead time $\tilde{T}$ of the compensation signal is tuned, the error signal originating from the initial step is compensated, and finally only shows a kink of one data sample at the position of the original signal.

Any further tuning of $\tilde{T}$ did not yield better results. I expect to reduce the remaining error signal by applying the Gaussian error function to the compensation signal, to simulate the response of the AOM. Nevertheless, this measurement shows that we are able to control the system in open loop, while still stabilizing in closed loop control to suppress fluctuations. The open loop approach increases the reaction speed tremendously, and is, in fact, only fundamentally limited by the AOM bandwidth. For the rise time measured above, the control bandwidth of the system is increased to $\omega_b \simeq 1/t_{\mathrm{r}} = 3.25\,\mathrm{MHz}$. This can in theory further be reduced by focusing the optical beam into the AOM, to minimize also the signal rise time.

Outlook: optimal control

In the first chapter we introduced the necessity to perform fast transport ramps in order to limit the motional excitation caused by the shift operation. Until now, all quantum walk experiments performed in our group have used the linear transport ramp according to the bang-bang technique [14], which is remarkably faster than adiabatic ramps without causing motional excitations of the atoms (see fig. 1.6 in sec. 1.3.3). These kinds of transport ramps should be well-executable with the improved bandwidth of the phase control loop.
Any further reduction of the transport time would, however, directly increase the number of coherent operations. As discussed in Robens [14, Chapter 3.4.2], the transport operation can be further improved by employing optimal control. In this approach, the phase and amplitude time trace are optimized to overlap the atom wave function before and after the transport operation,

while taking the system response function into account. With a well defined transport operation as shown above, the optimal control ramps can be further optimized to achieve even shorter translation times.

CHAPTER 4

Experimental realization of state-dependent transport

In the preceding chapters we have introduced and characterized the experimental setup to realize transport on a two-dimensional state-dependent optical lattice. In this last chapter, I will present the results we achieved utilizing the introduced hardware to transport atoms state-independently and state-dependently. In the first section, I will describe the electro-optical setup which we refer to as a polarization synthesizer, used in order to realize state dependent transport. The state-independent transport results were obtained without tge polarization synthesizer, meaning that the optical lattice is formed by lattice beams consisting of a single beam with linear polarization, corresponding to a zero spatial displacement between the two sub lattices; this results in an equal trapping potential for all atoms independent on their hyperfine state. Nevertheless, The results show that the transport mechanism works as intended.
As a last part of this thesis, I will present the first signature of state dependent transport.

4.1 The polarization synthesizer setup

In the following sections we will discuss the optical setup of the polarization synthesized lattice beams, and give an overview over the full experimental setup in order to provide background information on how the observations of atom transport were achieved. The optical setup is based on the already thoroughly tested configuration of the one-dimensional quantum walk experiment. Further informations can be found in references [27, 14].
At the heart of the polarization synthesizer lays the optical phase lock loop we introduced in section 3.2.3. With a well defined phase and amplitude of the light beam we can now introduce the polarization synthesis setup. To achieve an arbitrary polarization, two light beams – controlled as described in the previous chapter – are overlapped, to form a single light beam with controllable polarization as described in section 1.3. The full setup is displayed in figure 4.1.
A titanium sapphire laser provides the light for the polarization synthesized lattice beams. We separate a portion of the light with a beam splitter, which is used as a reference beam for the phase lock loop. Most of the linear polarized beam is sent through a half wave plate to rotate the polarization, such that it can be separated into two beams with equal intensity, but opposite linear polarization, by polarizing beam splitter cubes. Two two resulting, perpendicularly linear polarized beams (H,V for horizontal and vertical) are each modulated by an independent AOM

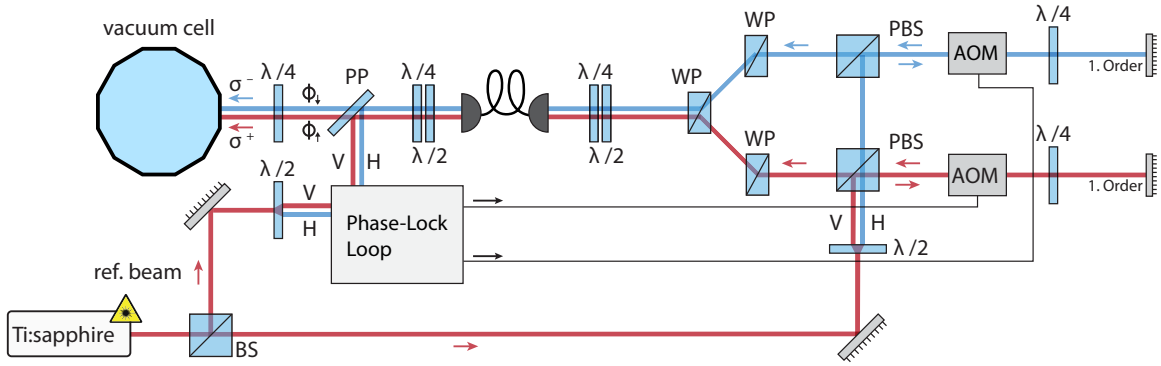

Figure 4.1: Optical setup schematic of the polarization synthesizer setup employed for two of the optical lattice beams. The light beam is produced by a Titanium-sapphire laser and distributed equally among the three lattice beams. Each lattice beam consists of two light beams stabilized as shown in fig. 3.11. Used abbreviations are Beam Splitter(BS), Half-wave Plate($\lambda/2$), vertical polarization(V), horizontal polarization(H), Polarizing Beam Splitter(PBS), Acousto-optic Modulator(AOM), Quarter-wave Plate($\lambda/4$), Wollaston Polarizer(WP) and Pickup Plate(PP). The phase lock loop electronics are drawn as a black box to reduce the complexity of the diagram.

in double pass configuration[1]; By steering the radio driving signal of the AOMs, stabilizing corrections are applied to the light field phase and amplitude. To combine the two components into one beam, we use two stages of Wollaston polarizers (WP). A Wollaston polarizer is a polarizing beam splitter, utilizing two calcite prisms with perpendicularly oriented optical axes. The use of two consecutive WPs further purifies the polarization state and makes the optical alignment process much easier, as the untypical separation angle of 19.2 degree is compensated by the second stage.
The overlapped optical beams are then coupled into a polarization maintaining optical fiber and sent to the main optical table, hosting the vacuum cell. A combination of quarter- and half-wave plates is used to align the angles of the two linear polarization to the optical axes of the fiber, to conserve the polarization to a high degree. After the fiber, the reference light for the phase and intensity lock is extracted by a pickup plate. The single mode optical fiber overlaps the two components into one spatial mode, such that there are no differential fluctuations on the remaining beam path. The two perpendicular horizontal polarization components are separated again by a Wollaston prism and fed into the fiber coupled phase lock loop photodiodes, where they create the phase lock beat signal together with the reference beam. This is where the degree of polarization of the two components plays a crucial role; if the polarization is not purely linear, the separated signals contain traces of the respective counterpart, leading to cross-talk between the two phase lock loops.
The main portion of the light is guided into the direction of the twelve sided vacuum cell (for details on this refer to Brakhane [65]). Directly in front of the vacuum cell the linear polarizations are converted by a quarter-wave plate to perpendicular circular polarizations with well defined phase $\phi_\uparrow, \phi_\downarrow$, respectively.
Comparing the results shown up to this point with the concept of polarization synthesis introduced in 1.3, we have met the requirements to synthesize an arbitrarily rotated linear polarization by applying a fixed amplitude and steering the phase of the two laser beams over

[1] The double pass configuration is chosen to increase the switching speed of the AOM, see Appendix for further details.

the digital phase lock loop.
The polarization synthesizer is further able to create an arbitrary polarized beam, as laid out in detail in [27]. Following the derivations in this publication, the root mean square errors of the state of polarization (SOP) on the Poincaré sphere can be calculated from the cumulative phase jitter and relative intensity noise $\Delta\phi$ and $\Delta I/I$ of the polarization synthesized light, respectively (see sections 3.2.3 and 3.2.2). These values are related to the root mean square uncertainties of the SOP by

$$\langle\psi\rangle = \Delta\phi, \tag{4.1}$$

$$\langle\chi\rangle = \tan^{-1}\left(\frac{\Delta I}{I}\right), \tag{4.2}$$

where ψ and χ are the azimuthal and polar angle on the Poincaré sphere (see sec. 1.3). The corresponding values are summarized in table 4.1. The table lists also a best case scenario SOP*, for which the dominant noise peak caused by the TiSa-etalon lock is neglected. This data shows a good agreement with the nominal SOP uncertainty given in [27] ($\mathrm{SOP}_{\mathrm{nom}}$)

Table 4.1: Precision limitations of the synthesized polarization: intensity noise and phase noise. The SOP is given for both angular coordinates, for both polarization synthesized beams HDT 1 and HDT 2 and best case scenario (SOP*). The data is compared to the nominal values $\mathrm{SOP}_{\mathrm{nom}}$ of the corresponding publication.

	SOP (HDT 1)	SOP(HDT 3)	SOP*	$\mathrm{SOP}_{\mathrm{nom}}$
phase noise	$\langle\psi\rangle = 0.17°$	$\langle\psi\rangle = 0.1°$	$\langle\psi\rangle = 0.05°$	$\langle\psi\rangle = 0.1°$
intensity noise	$\langle\chi\rangle = 0.13°$	$\langle\chi\rangle = 0.09°$	$\langle\chi\rangle = 0.025°$	$\langle\chi\rangle = 0.025°$

4.2 Setup for polarization synthesis in two dimensions

While a detailed setup overview of the entire experimental apparatus is out of the scope of this thesis, the general operation can be introduced. The experimental setup revolves around the twelve sided, in-house manufactured vacuum cell developed by Stefan Brakhane [66]. A simplified version of the setup is illustrated in figure 4.2 a. The setup employs in total two of the polarization synthesized beams, each phase and amplitude controlled by an identical version of the digital stabilization setup. The two dimensional interference pattern is created in combination with the perpendicular, linear polarized beam (see chapter 1.3). The full setup consists of a variety of additional systems to realize the operation of the experiment, the explanation of which is however out of the scope of this thesis. The detailed description of the development and assembly can be found in Brakhane [13].
The experiment follows a more or less static experimental sequence. As a first step, neutral cesium atoms from the background of the vacuum chamber are trapped in a magneto-optical trap, located in a distance of about 1 mm from the imaging system. After the number of trapped atoms has reached a satisfactory value, the ensemble is moved by shifting the magnetic quadrupole field towards the lattice position. The three lattice beams are aligned to form the optical lattice potential at the imaging plane in a distance of 150 µm from a high NA objective [66]. With a numerical aperture of NA = 0.92 the imaging system reaches single

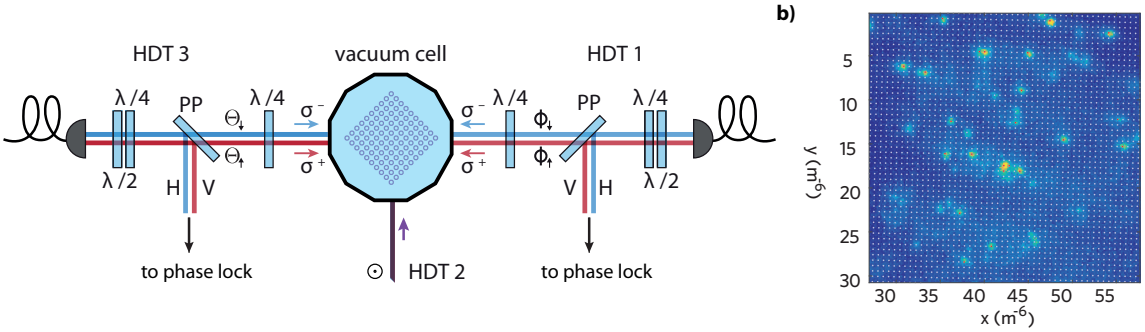

Figure 4.2: Overview of the experimental setup. a) shows the orientation of the two polarization synthesized lattice arms with respect to the vacuum cell and the reference beam. The graphic is a simplified illustration of the experimental setup, as it neglects optical beam paths for molasses cooling, trapping beams of the MOT, gradient coils, magnetic shielding, imaging system, and the microwave setup. b) Example of the experimental data available at this state of the experiment. The high NA objective takes single site resolved pictures of the atoms located in the lattice.

site resolution, where the distance between two lattice positions corresponds to a four pixel separation on the resulting image. An example of the images taken is shown in figure 4.2 b. The imaging system is aligned such that the dimensions of the image overlap with the lattice translation directions which are rotated by 45° with respect to the beam alignment (see sec. 1.1). The image shows the theoretical lattice sites as gray dots, as they have been inferred from the atom positions [13]. During the experimental sequence we take between two to a few tens of images, while performing operations on the atoms in between each picture.

4.3 Experimental transport results

4.3.1 State-independent transport

The state-independent transport results were achieved in the early phase of this thesis, where the implementation of the synthesized polarizations was still not completed. All of the lattice beams consist therefore only of a single beam of linear polarization – therefore addressing all spin states equally. The phases ϕ, Θ of the counterpropagating beams can already be varied to achieve deterministic transport, although no phase stabilization is active – with only one beam, the interferometric effect causing the differential phase noise is not present, such that the lattice position noise is governed by the phase noise of the radio signal and intrinsic laser noise. These effects are insignificant enough to allow to take multiple pictures during the duration of the experimental sequence. This reduces the light-pollution of the pictures and makes it possible to track the movement of individual atoms at a time. Figure 4.3 shows the first six steps of a twelve step transport operation. The atoms are in this case transported by four lattice sites by ramping the phase ϕ of HDT 1 by 8π in a sinusoidal manner in between each picture, which corresponds to a transport of 4 lattice sites. After four consecutive pictures the transport direction is changed and the respective other phase Θ of HDT 2 is ramped instead. This changes the transport direction by 90°. In the original measurement, the directions are reversed and the

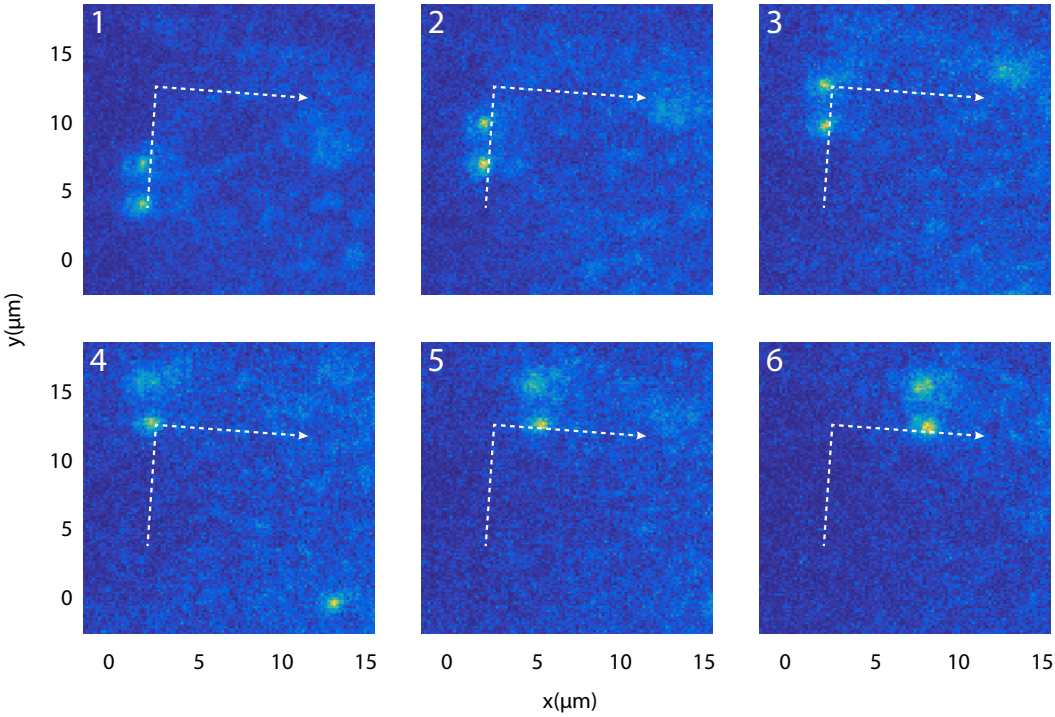

Figure 4.3: Experimental data of state independent transport in two orthogonal dimensions. The atoms are transported by four lattice sites per step. The pixel values have been converted to micrometers by assuming 1 px = 154nm [13, chapter 4.3.2]. The white arrow marks the path of the lower atom.

atom is transported back to the original position, completing a full square path[2].

4.3.2 State-dependent transport

In order to observe a signature of state dependent transport, we have to prepare state of the atoms by means of optical pumping. The repump light of the magneto-optical trap uses the cesium D_2-line and prepares the atoms in $|F = 4\rangle$. It can be σ^+ polarized, as it enters the vacuum chamber on the lattice beam path of the polarization synthesized beams, which in turn prepares the atoms in $|F = 4, m_F = 4\rangle$ – the spin-up state of our pseudo-spin 1/2 system. We can achieve a statistical mixture of spin states by storing the atoms in the lattice for a given time before applying the shift operation. During this time the spin decoherence will first populate the $|F = 3, m_F = 3\rangle$ state, and subsequently all other hyperfine ground states. To observe spin dependent transport, we program a lattice translation of ten lattice sites in opposite directions depending on the spin. The measurement shown in figure 4.4 shows two atoms moving in such a way, traveling a distance of 40 pixels (or 6.1 µm). This corresponds precisely to the programmed distance.

[2] The full movie is available at [67]

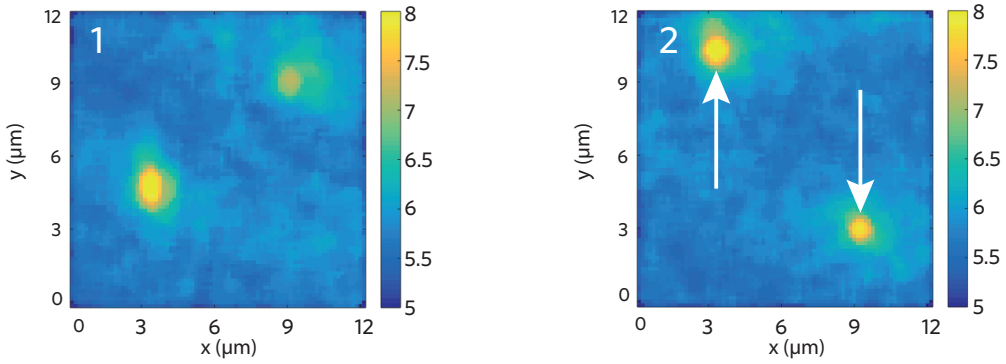

Figure 4.4: Experimental data of state dependent transport in one dimension. Areas of high camera ccd counts are color-coded in yellow, areas with low counts in blue. The scale has been logarithmically plotted to enhance the contrast. The atoms are transported by ten lattice sites, corresponding to 40 pixels or 6.16µm. The dimensions have been converted to micrometers by using the conversion 1 px = 154 nm [13]. The two state dependent potentials are moved in opposite directions, such that we can infer the states of the atoms to be orthogonal.

Summary and Outlook

Summary

In this thesis, I have presented the implementation and characterization of a digital control system tailored specifically for the requirements of optical phase and intensity control loops of laser beams. The control bandwidth and the stabilization capability of the digital lock has been characterized and shown to be on par with the formerly used digital control system. I designed the control system on the FPGA platform of the vector generator, utilizing the basic control tools provided by the Signadyne software, and included a feedforward control capability, using internal model control inspired by the Smith predictor.
The digital control loops have been implemented into the main experimental apparatus to realize two polarization synthesized laser beams, and the device has been included in the experiment controller software, such that it is ready to use within the existing interface. Finally, the inclusion into the optical setup allowed us to observe the first signature of atom transport by deterministically translating the optical lattice.

Outlook

This thesis presented the application of a digital control system in order to transport atoms in an optical lattice. In the following chapter, I will give a brief overview of the immediate goals of the two dimensional quantum walk experiment.

The immediate next steps to be taken with regard to the control loops of the lattice are the full inclusion of the feedforward control into the transport operation of the apparatus. Our goal is to completely integrate the operation into the experiment controller, such that the operation is automated after an initial tuning process. This would, in turn, enable the use of optimal control ramps to maximize the speed and minimize excitations during transport operations. Furthermore, we plan an extension of the feedforward control to include also the intensity lock, such that the depth of the lattices can too be controlled with increased bandwidth.

Minor goals regarding the digital control system are the inclusion of automated tuning of step responses by utilizing the digital data acquisition system. Minor changes to the FPGA-firmware would enable to directly record the response of the system using the feedback signal, such that the tuning of the system could be performed directly from the main laboratory computer. There are also plans to implement safety measures into the general FPGA firmware to monitor the lock signals during experimental sequences. This way, possibly disturbed or compromised runs could be detected and post-selectively excluded.

Besides state-dependent transport, the spin manipulation of atoms is one of the main methods to perform two-dimensional quantum walks. One of the key tools in the experimental apparatus are coherent microwave operations, which enable to drive transitions between the qubit spin-states. Figure 4.5 shows the recently observed Rabi oscillations, which were achieved by driving spin rotations of the atoms with microwave pulses of varying length. The measurement depicts

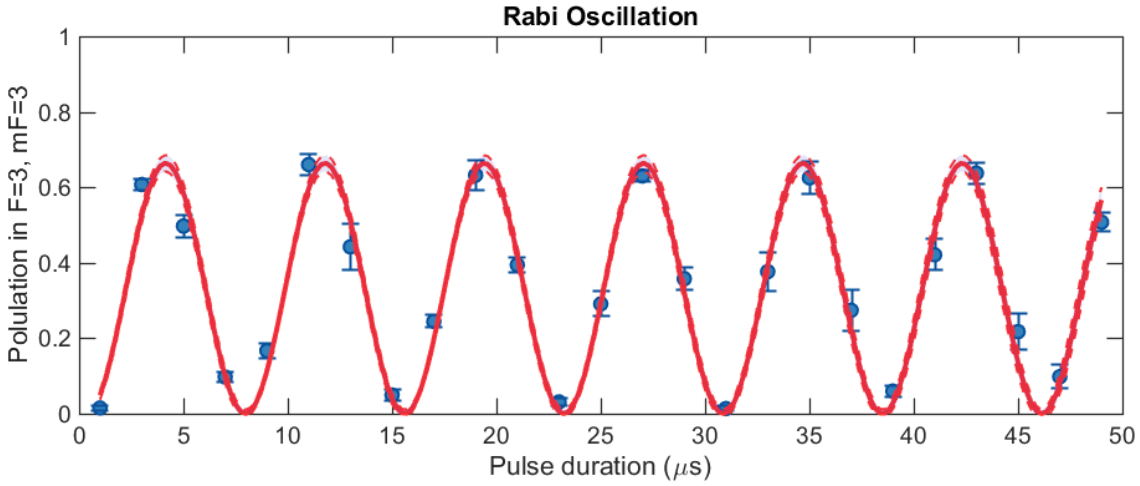

Figure 4.5: Rabi oscillations of the spin population of the cesium atoms. Blue dots indicate measured data, while the red line is a fitted sinusoidal function with confidence intervals displayed as dashed lines. The Rabi oscillation frequency amounts to 131 kHz.

the population of the $|\downarrow\rangle$-state, which oscillates with a contrast of 0.65 and a frequency of 131(1) kHz. The microwave allows us to deterministically prepare our spin-states prior to performing spin dependent transport, in contrast to the spin-dependent transport shown in section 4.3.2. With integrated ground state cooling and the ability to measure the population of atoms in the lowest vibrational states through microwave, we could directly observe the excitations caused by the transport operation.

Using the digital control platform, we will perform state-dependent transport and quantum walks, where we will use internal model control to steer the lattice with transport ramps calculated using optimal control theory. The two dimensional quantum walk is the building block for many experimental schemes. Proposals for an atom sorting algorithm have been laid out in a recent publication of our group, which crucially rely on the transport operation [68]. With the now implemented transport operation, we expect to be able to create a lattice section as large as 31x31 sites with unity filling.

Lastly, the transport operation is one of the steps to take towards the observation of topologically protected edge states, the concept of which was laid out and in Groh [19]. The experimental realization of this concept requires the state dependent transport operation, as well as the implementation of a spatially resolved spin-flip operator. The former is now implemented as a result of the work presented in this thesis, the latter has been investigated in a recent master thesis of Alexander Knieps [69], and is planned to be implemented to the experimental apparatus within the next months.

Acknowledgements

During the year I spent working in the group of professor Meschede, I had the chance to get to know a number of outstanding people who really made my time in this group a memorable experience. I want to sincerely thank all the people who continuously supported me during the course of my work on this project and from whom I was able to learn so much. First and an foremost, I want to thank Professor Meschede, who gave me the opportunity to work in this exciting field of physics by joining his research group. In addition, his continuous support to participate and present my work in the various conferences during this year made the time spent on this project an even more fascinating learning experience. Also, I would like to thank Professor Weitz, who kindly agreed to be my second supervisor.

Dr. Andrea Alberti, who suggested this exciting topic for my Master thesis. I was always amazed how somebody who is obviously involved in numerous projects of wider scope, was still so genuinely interested and happy to discuss even the most technical problems, and provided me with so much background information.

Dr. Wolfgang Alt, who was of great help in every discussion we had, and always gave me clear and helpful feedback for both my poster and my colloquium.

I also want to thank Carsten Robens and Stefan Brakhane, who were always available to help me out, despite being occupied with writing up their PhD. theses. I am truly thankful for all the advice and effort they showed during my work in the lab, as well as the time I spent writing my thesis.

Gautam, Geol and Richard, who I spend a lot of time with in the lab and who helped me to learn the experimental techniques I needed. They were always around to help me out, which was of great comfort to me.

Also, I have to thank José Gallego, whit whom I shared an office for the last weeks to work on my thesis. For me it was a lot easier to commit to the writing schedule with someone who was in a similar situation.

I also got to spend a lot of time with some of the people of this group outside the lab, which I think is not necessarily common, and was really great. Besides work, I was able to also talk about drones, microprocessors, video games and neural networking, which made the work environment friendly and enjoyable.

I also want to thank my friends from in- and outside of this group, who also deserve to be acknowledged for the support they provide in my life.

Lastly, I want to thank my parents for supporting me not only throughout my Master, but for all the course of my studies.

Bibliography

[1] T. H. MAIMAN and T. H., *Stimulated Optical Radiation in Ruby*, Nature **187** no. 4736, (1960) 493–494, http://www.nature.com/doifinder/10.1038/187493a0.

[2] A. L. Schawlow and C. H. Townes, *Infrared and Optical Masers*, Phys. Rev. **112** no. 6, (1958) 1940–1949, http://link.aps.org/doi/10.1103/PhysRev.112.1940.

[3] T. W. Hänsch and A. L. Schawlow, *Cooling of gases by laser radiation*, Optics Communications **13** no. 1, (1975) 68–69, http://www.sciencedirect.com/science/article/pii/0030401875901595.

[4] H. F. Hess, *Evaporative cooling of magnetically trapped and compressed spin-polarized hydrogen*, Phys. Rev. B **34** no. 5, (1986) 3476–3479, http://link.aps.org/doi/10.1103/PhysRevB.34.3476.

[5] M. H. Anderson, J.R. Eshner, M. R. Matthews, C. E. Wieman and E. A. Cornell, *Observation of Bose-Einstein-Condensation in a Dilute Atomic Vapor*, Science 269 **198** (1995).

[6] K. B. Davis, M. O. Mewes, M. R. Andrews, N. J. van Druten, D. S. Durfee, D. M. Kurn and W. Ketterle, *Bose-Einstein condensation in a Gas of Sodium Atoms*, Phys. Rev Lett. 75 **3969** (1995).

[7] A. Einstein, *Quantentheorie des einatomigen idealen Gases*, Sitzungsberichte der preussischen Akademie der Wissenschaften **261** (1924).

[8] A. Einstein, *Quantentheorie des einatomigen idealen Gases: Zweite Abhandlung*, Sitzungsberichte der preussischen Akademie der Wissenschaften **3** (1925).

[9] S. N. Bose, *Plancks Gesetz und Lichtquantenhypothese*, Z. Phys. 26 **178** (1924).

[10] R. P. Feynman, *Quantum Mechanical Computers*, Optics News **11** no. 2, (1985) 11–20, http://www.osa-opn.org/abstract.cfm?URI=on-11-2-11.

[11] M. Ben Dahan, E. Peik, J. Reichel, Y. Castin, and C. Salomon, *Bloch Oscillations of Atoms in an Optical Potential*, Phys. Rev. Lett. **76** no. 24, (1996) 4508–4511, http://link.aps.org/doi/10.1103/PhysRevLett.76.4508.

[12] T. Rakovszky, J. Asbóth, and A. Alberti, *Detecting topological invariants in chiral symmetric insulators via losses*, arXiv:1611.09670 (2016).

[13] S. Brankhane, *The quantum walk microscope*, PhD Thesis (2016), http://quantum-technologies.iap.uni-bonn.de/de/phd-thesis.html?task=download&file=309&token=57dad9f140b1e7d06600262d0409b3b4.

[14] C. Robens, *Testing the Quantumness of Atom Trajectories*, 2016.

[15] M. Genske, W. Alt, A. Steffen, A. H. Werner, R. F. Werner, D. Meschede, and A. Alberti, *Electric quantum walks with individual atoms*, Phys. Rev. Lett. **110** (2013) 190601.

[16] C. Robens, J. Zopes, W. Alt, S. Brakhane, D. Meschede, and A. Alberti, *Low-entropy states of neutral atoms in polarization-synthesized optical lattices*, arXiv:1608.02410v2 (accepted in Phys. Rev. Lett.) (2016).

[17] G. Di Molfetta, *Discrete time quantum walks : from synthetic gauge fields to spontaneous equilibration*. Theses, Universit{é} Pierre et Marie Curie - Paris VI, 2015. https://tel.archives-ouvertes.fr/tel-01230891.

[18] C. Robens, W. Alt, D. Meschede, C. Emary, and A. Alberti, *Ideal Negative Measurements in Quantum Walks Disprove Theories Based on Classical Trajectories*, Phys. Rev. X **5** (2015) 11003.

[19] T. Groh, S. Brakhane, W. Alt, D. Meschede, J. Asbóth, and A. Alberti, *Robustness of topologically protected edge states in quantum walk experiments with neutral atoms*, Phys. Rev. A (editor's suggestion) **94** (2016) 13620.

[20] D. J. Thouless, M. Kohmoto, M. P. Nightingale, and M. den Nijs, *Quantized Hall Conductance in a Two-Dimensional Periodic Potential*, Phys. Rev. Lett. **49** no. 6, (1982) 405–408, http://link.aps.org/doi/10.1103/PhysRevLett.49.405.

[21] H. B. Perets, Y. Lahini, F. Pozzi, M. Sorel, R. Morandotti, and Y. Silberberg, *Realization of Quantum Walks with Negligible Decoherence in Waveguide Lattices*, Phys. Rev. Lett. **100** no. 17, (2008) 170506, http://link.aps.org/doi/10.1103/PhysRevLett.100.170506.

[22] M. Karski, L. Förster, J. Choi, A. Steffen, W. Alt, D. Meschede, and A. Widera, *Quantum Walk in Position Space with Single Optically Trapped Atoms*, Science **325** (2009) 174.

[23] H. Schmitz, R. Matjeschk, C. Schneider, J. Glueckert, M. Enderlein, T. Huber, and T. Schaetz, *Quantum Walk of a Trapped Ion in Phase Space*, Phys. Rev. Lett. **103** no. 9, (2009) 90504, http://link.aps.org/doi/10.1103/PhysRevLett.103.090504.

[24] D. E. Kirk, *Optimal control theory an introduction*, 1970. http://opac.inria.fr/record=b1108761.

[25] A. Negretti, C. Robens, W. Alt, D. Meschede, T. Calarco, G. Ramola, and Alberti, *Optimal and fast transport control for coherent splittings of trapped atoms*,.

[26] M. Karski, *State-selective transport of single neutral atoms*. Dissertaion, 2010.

[27] C. Robens, S. Brakhane, W. Alt, D. Meschede, J. Zopes, and A. Alberti, *Fast, high-precision optical polarization synthesizer for ultracold-atom experiments*, arXiv **1611.07952** (2016) 1–9, arXiv:1611.07952, http://arxiv.org/abs/1611.07952.

[28] W. Alt, *Optical control of single neutral atoms*. Phd, 2004. http://quantum-technologies.iap.uni-bonn.de/de/component/publications/?task=download&file=63&token=1ab669075fd52a95bdd3c662e9178601.

[29] R. Grimm, M. Weidemüller, and Y. B. Ovchinnikov, *Optical dipole traps for neutral atoms*, Advances In Atomic, Molecular, and Optical Physics Volume 42. Series: Advances In Atomic, Molecular, and Optical Physics, ISBN: 9780120038428. Elsevier, vol. 42, pp. 95-170 **42** (1999) 95–170, arXiv:9902072 [physics], http://arxiv.org/abs/physics/9902072.

[30] C. Robens, S. Brakhane, D. Meschede, and A. Alberti, *Quantum Walks with Neutral Atoms: Quantum Interference Effects of One and Two Particles*, pp. , 1–15. WORLD SCIENTIFIC, Dec, 2016. http://www.worldscientific.com/doi/abs/10.1142/9789813200616_0001.

[31] C. Robens, J. Zopes, W. Alt, S. Brakhane, D. Meschede, and A. Alberti, *Low-entropy states of neutral atoms in polarization-synthesized optical lattices*, arXiv:1608.02410, http://arxiv.org/abs/1608.02410.

[32] D. A. Steck, *Cesium D Line Data*, http://steck.us/alkalidata/cesiumnumbers.1.6.pdf.

[33] M. Bass, *Handbook of Optics, Volume II - Devices, Measurements, and Properties*,.

[34] Crystal Technologies, *AOMO 3080-122 Datasheet*, 2003.

[35] Schäfter&Kirchhoff, *Fiber Collimators 60FC-...*, http://www.sukhamburg.com/download/fk60fc_e.pdf.

[36] Miller, Cline, and Heinzen, *Far-off-resonance optical trapping of atoms.*, Physical review. A, Atomic, molecular, and optical physics **47** no. 6, (1993) R4567–R4570, http://www.ncbi.nlm.nih.gov/pubmed/9909564.

[37] M. E. Gehm, K. M. O'Hara, T. A. Savard, and J. E. Thomas, *Dynamics of noise-induced heating in atom traps*, Physical Review A **58** no. 5, (1998) 3914–3921, https://link.aps.org/doi/10.1103/PhysRevA.58.3914.

[38] T. A. Savard, K. M. O 'hara, and J. E. Thomas, *Laser-noise-induced heating in far-off resonance optical traps*, https://physics.ncsu.edu/jet/publications/pdf/LaserNoise.pdf.

[39] *IEEE Standard Definitions of Physical Quantities for Fundamental Frequency and Time Metrology— Random Instabilities IEEE-SA Standards Board*, http://www.photonics.umbc.edu/Menyuk/Phase-Noise/Vig_IEEE_Standard_1139-1999.pdf.

[40] S. Blatt, A. Mazurenko, M. F. Parsons, C. S. Chiu, F. Huber, and M. Greiner, *Low-noise optical lattices for ultracold Li 6*, Physical Review A **92** no. 2, (2015) 021402, https://link.aps.org/doi/10.1103/PhysRevA.92.021402.

[41] A. Hambitzer, *Direct Synthesis of Light Polarization for State-Dependent Transport*,.

[42] Signadyne.com, *Signadyne AIO-H3335/6 F Datasheet*, https://www.signadyne.com/contenido/documentation/files/2601/sd_aio_h3335_6_f_datasheet.pdf.

[43] K. Warwick and D. Rees, *Industrial Digital Control Systems, 2nd Edition*. I E E Control Engineering Series, 2 ed., 1988.

[44] W. G. Jung, *Op amp applications*, 2002. http://www.analog.com/en/analog-dialogue/articles/adc-input-noise.html.

[45] P. Symons, *Digital Waveform Generation*. Cambridge University Press, Cambridge, 2013. http://ebooks.cambridge.org/ref/id/CBO9781139108072.

[46] *Tutorial - Fundamentals of Direct Digital Synthesis (DDS)*, Analog Devices, http://www.analog.com/media/en/training-seminars/tutorials/MT-085.pdf.

[47] J. Vankka, *Direct digital synthesizers : theory, design and applications*. PhD thesis, Helsinki University of Technology, 2000. http://lib.tkk.fi/Diss/2000/isbn9512253186/.

[48] R. P. Scott, C. Langrock, and B. H. Kolner, *High-dynamic-range laser amplitude and phase noise measurement techniques*, Ieee Journal of Selected Topics in Quantum Electronics **7** no. 4, (2001) 641–655.

[49] G. Ramola, *A versatile digital frequency synthesizer for state-dependent transport of trapped neutral atoms*. Master thesis, 2015.

[50] K. J. Aström, *Lecture Notes: Control System Design - Chapter 6: PID Control*, https://www.cds.caltech.edu/~murray/courses/cds101/fa02/caltech/astrom.html.

[51] P.-D. Eversheim, *Lecture Notes: Systemanalysis with Laplacetransformation*, http://veversheim.hiskp.uni-bonn.de/ws1516/vorlesungen/electronics/.

[52] K. J. Aström, *Lecture Notes: Control System Design - Chapter 3: Dynamics*, https://www.cds.caltech.edu/~murray/courses/cds101/fa02/caltech/astrom.html.

[53] D. Trumper, *Analysis and Design of Feedback Control Systems | Mechanical Engineering | MIT OpenCourseWare*, 2014. https://ocw.mit.edu/courses/mechanical-engineering/2-14-analysis-and-design-of-feedback-control-systems-spring-2014/{#}.

[54] K. Ogata, *Modern Control Engineering*. Prentice Hall PTR, Upper Saddle River, NJ, USA, 4th ed., 2001.

[55] K. J. Aström, *Lecture Notes: Control System Design - Chapter 4: Simple Controllers*, https://www.cds.caltech.edu/~murray/courses/cds101/fa02/caltech/astrom.html.

[56] Signadyne, *Signadyne PID IP Datasheet*,.

[57] Coherent, *Mbr-110 Service Manual*, 2002.

[58] Emhiser, *Mixer Application Guide*, http://www.emhiser.com/images/content/121/ETTI-_Mixer_Application_Guide.pdf.

[59] *Signadyne PLL IP v1.1*, 2015.

[60] A. Visioli and Q. Zhong, *Control of Integral Processes with Dead Time*. Advances in Industrial Control. Springer London, London, 2011. http://link.springer.com/10.1007/978-0-85729-070-0.

[61] D. Rivera, *Internal model control: a comprehensive view*, Arizona State University (1999), http://www.eq.ufrj.br/links/h2cin/eqe709/AULA_6/RIVERA.pdf.

[62] K. Warwick and D. Rees, *Industrial digital control systems*. Peter Peregrinus Ltd. on behalf of the Institution of Electrical Engineers, 1988.

[63] F. Seidler, *Digital high bandwidth feedback controller*,.

[64] A. Alberti, *Private conversation*,.

[65] S. Brakhane, W. Alt, D. Meschede, C. Robens, G. Moon, and A. Alberti, *Note: Ultra-low birefringence dodecagonal vacuum glass cell*, Review of Scientific Instruments **86** no. 12, (2015) 126108, http://aip.scitation.org/doi/10.1063/1.4938281.

[66] C. Robens, S. Brakhane, W. Alt, F. Kleißler, D. Meschede, G. Moon, G. Ramola, and A. Alberti, *A high numerical aperture (NA = 0.92) objective lens for imaging and addressing of cold atoms*, arXiv:1611.02159 (2016).

[67] DQSIM, *2D Atom transport movie*, 2016. https://drive.google.com/file/d/0B_MNVJWydrNCYmZJajE3eEF1bUE/view.

[68] C. Robens, J. Zopes, W. Alt, S. Brakhane, D. Meschede, and A. Alberti, *Low-entropy states of neutral atoms in polarization-synthesized optical lattices*, arXiv:1608.02410v2 (2016).

[69] A. Knieps, *A Spatial Light Modulator for Steering Quantum Walks with Single Site Precision*. Master thesis, 2017.

Appendix

APPENDIX A

Useful information

Improvement of the FPGA-firmware

In section 2.1.4 I already mentioned one of the techniques that could be used in the future to simplify the operation of the lattice beams. During the work on the firmwares of the FPGA I started a couple of projects, which offered nice utility but were in the end not necessary for the experimental operation and thus never got finalized. In this section I briefly want to go over them and the utilities that they could offer.

- **Internal triggering:** As mentioned in section 2.1.4, the data acquisition structure on the FPGA is able to trigger to a threshold value of any data stream on the module. This functionality could be used to automatically tune any of the PID-controllers at the press of a button. The basic principle was already used out of necessity to observe the data presented in section 3.3.3, as the PLL error signal is only accessible on the FPGA. However, applying this method to every channel of the module, the transient response of the corresponding controllers could be measured directly – sparing the time to optically observe the signal or split the data provided by the in-loop photodiode.
- **Internal model control: intensity** The execution of the optimal control transport ramps requires not only the fast ramping of the phase, but also of the intensity. This could be achieved by routing another AWG data line to the intensity lock and replicating the phase lock scheme there. However, this would mean to strip the modulation functionality completely from the remaining two output channels, as the AWGs would be occupied by the control loops.
- **sharing AWG data:** To counteract the usage of additional AWG streams – which reduces the modulation functionality of the remaining output channels – the firmware can be optimized to use one AWG data stream for multiple purposes. An example would be the intensity setpoint: This setpoint is currently only changed when the depth of the lattice is changed, and it changes equally for all intensity locks. In the current configuration, both components of a synthesized lattice beam are controlled from one Signadyne module. The AWG usage could be reduced by using one setpoint for both of the intensity locks.

Double pass AOM configuration

The double pass AOM configuration is implemented after we noticed a drift in the intensity after switching the AOM from low to high powers. We concluded the high power led to a heating

of the crystal, which in turn changed the beam path and corrupted the fiber coupling, which in turn led to a drop of intensity after the fiber. To counteract this, we changed the setup to include a refraction angle independent double pass configuration, since the low intensity over a duration of a couple of seconds caused the intensity locks to oversteer and wind up.